JACS
JOURNAL OF THE AMERICAN CHEMICAL SOCIETY
Article
pubs.acs.org/JACS

Aqueous-Phase Preparation of Model HDS Catalysts on Planar Alumina Substrates: Support Effect on Mo Adsorption and Sulfidation

Cédric Bara,[†,‡] Lucie Plais,[†] Kim Larmier,[†,‡] Elodie Devers,[‡] Mathieu Digne,[‡] Anne-Félicie Lamic-Humblot,[†] Gerhard D. Pirngruber,[‡] and Xavier Carrier*[,†]

[†]Sorbonne Universités, UPMC Univ Paris 06, CNRS, Laboratoire de Réactivité de Surface, F-75005 Paris, France
[‡]IFP Energies nouvelles, BP3, Rond Point Échangeur de Solaize, F-69360 Solaize, France

Supporting Information

ABSTRACT: The role of the oxide support on the structure of the MoS_2 active phase (size, morphology, orientation, sulfidation ratio, etc.) remains an open question in hydrotreating catalysis and biomass processing with important industrial implications for the design of improved catalytic formulations. The present work builds on an aqueous-phase surface-science approach using four well-defined α-alumina single crystal surfaces (C (0001), A ($11\bar{2}0$), M ($10\bar{1}0$), and R ($1\bar{1}02$) planes) as surrogates for γ-alumina (the industrial support) in order to discriminate the specific role of individual support facets. The reactivity of the various surface orientations toward molybdenum adsorption is controlled by the speciation of surface hydroxyls that determines the surface charge at the oxide/water interface. The C (0001) plane is inert, and the R ($1\bar{1}02$) plane has a limited Mo adsorption capacity while the A ($11\bar{2}0$) and M ($10\bar{1}0$) surfaces are highly reactive. Sulfidation of model catalysts reveals the highest sulfidation degree for the A ($11\bar{2}0$) and M ($10\bar{1}0$) planes suggesting weak metal/support interactions. Conversely, a low sulfidation rate and shorter MoS_2 slabs are found for the R ($1\bar{1}02$) plane implying stronger Mo−O−Al bonds. These limiting cases are reminiscent of type I/type II MoS_2 nanostructures. Structural analogies between α- and γ- alumina surfaces allow us to bridge the material gap with real Al_2O_3-supported catalysts. Hence, it can be proposed that Mo distribution and sulfidation rate are heterogeneous and surface-dependent on industrial γ-Al_2O_3-supported high-surface-area catalysts. These results demonstrate that a proper control of the γ-alumina morphology is a strategic lever for a molecular-scale design of hydrotreating catalysts.

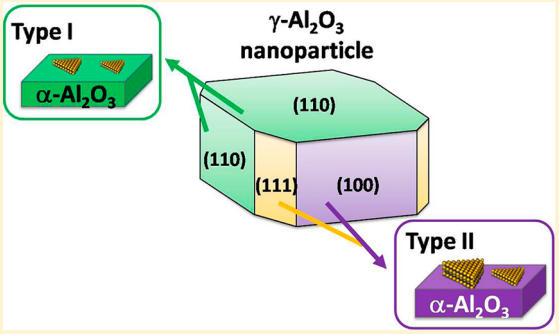

INTRODUCTION

Heterogeneous catalysts based on transition metal sulfides (TMSs) are key players to face current environmental challenges related to gas emission or biofuel production. Indeed, TMSs have been used for more than 70 years in the refining industry as hydrotreating catalysts (HDTs) to remove contaminants (S, O, N, and metals) from crude oil with a special environmental concern on sulfur removal through hydrodesulfurization (HDS).[1] They are also used as catalysts to hydrogenate renewable fats from vegetable oils into oxygen-free diesel bases (UOP Ecofining or Axens Vegan processes) and are potential candidates for upgrading bio-oils derived from pyrolysis of second generation lignocellulosic biomass in order to reduce their oxygen content (hydrodeoxygenation) and increase the engine efficiency.[2]

Constant improvements in the design and composition of TMS-based heterogeneous catalysts have been driven by more and more stringent environmental specifications (namely for the maximum allowable sulfur content in fuels[3]) and have led to a massive amount of research in the field from the 1970s.[1,4,5] Nowadays, a broad consensus exists on the structure of TMS-based catalysts which can be described as made of Mo(W)S_2 nanosheets decorated by promoter atoms (Co or Ni) at the edge of the sheets that are dispersed on high-surface-area oxide supports (mostly alumina).[6] However, despite more than 40 years of research, the exact role of the oxide support (also known as support effect) on the structure of the TMS active phase (size, morphology, orientation, sulfidation rate, etc.) remains an open question with important industrial implications since a detailed understanding of this support effect could help in the design of new or improved catalytic supports.

Several hypotheses have been put forward to explain the influence of different supports (Al_2O_3, SiO_2, TiO_2, ZrO_2, carbon, etc.) on the HDT catalytic activity including the following:[7,8] (i) the existence of specific metal−support interactions that may dictate the orientation of the active phase and/or the sulfidation rate or (ii) the participation of acid/base sites that influence the electronic structure of the TMS active phase. As an example, titania has been shown to be

Received: October 20, 2015
Published: November 20, 2015

DOI: 10.1021/jacs.5b10975
J. Am. Chem. Soc. 2015, 137, 15915−15928

a very interesting support since TiO_2-supported Mo catalysts are 4−5 times more active than their alumina counterpart. One recurring explanation involves the existence of an epitaxial relationship between the MoS_2 phase and the support[9,10] that will promote selective edge-bonding of supported MoS_2 nanoslabs to the surface and favor high Mo-edge/S-edge ratio as well as sulfur-deficient particles.[10] As for alumina, a recent study by Laurenti et al.[11] showed a distinct behavior (intrinsic activity in thiophene HDS and selectivity) for various alumina polymorphs (γ_{cubic}, $\gamma_{tetragonal}$, and δ). The higher intrinsic activity for δ-Al_2O_3 was related to a higher dispersion of the active phase and lower metal−support interactions.

The origin of such differences may lie in the fact that the various Al_2O_3 polymorphs expose different types of surfaces. However, the specific role of different alumina surfaces has been only very scarcely investigated in the literature.

We have recently underlined[9] that a molecular-scale understanding of the support effect may largely benefit from model studies using planar and oriented single crystal surfaces. Such a surface-science approach can help discriminate the specific role of individual support orientations which is precluded with oxide powders exposing several surfaces with different prevalence according to the synthesis route. However, addressing this support effect with planar substrates requires us to work with insulating oxide surfaces that impose constraints on the use of electron-based techniques such as STM for example while it has been used with great benefit on metallic[12,13] or semiconducting surfaces.[14] Nevertheless, the use of model oxide substrates has already proven to be highly beneficial since a previous surface-science study from Sakashita et al.[15] on oriented alumina thin films demonstrated, with the help of transmission electron microscopy (TEM), a surface-dependence on the sulfidation rate and orientation of Al_2O_3-supported MoS_2 nanostructures. However, the samples had to suffer a quite harsh mechanical treatment before TEM observation which raises some concern about the nature and orientation of the surfaces investigated. Moreover, Mo deposition was carried out through MoO_3 vacuum evaporation which is far from the aqueous-phase deposition favored for industrial catalysts. In fact, Sterrer and Freund[16] recently highlighted that wet impregnation in surface-science studies is a key step forward in order to integrate the influence of support hydroxylation that may be crucial for controlling nucleation and growth of the active phase.

Hence, the present work addresses the support effect of different alumina orientations by using (i) well-defined single crystal alumina wafers of different orientations and (ii) aqueous-phase deposition of the active phase that is closer to industrial practice (mainly incipient wetness impregnation) and permits us to include the complexity of the oxide/water interface as opposed to the UHV-type surface-science deposition methods.[9] α-Al_2O_3 single crystal wafers with four different surface orientations, A $(11\bar{2}0)$, C (0001), M $(10\bar{1}0)$, and R $(1\bar{1}02)$, have been chosen since they show a well-ordered surface structure (i.e., few or no defects), a well-defined number of surface sites, and they can be used as a model for γ-alumina (the most industrially relevant polymorph in HDT catalysis) that is unfortunately not available as macroscopic single crystal wafers.[9]

We have already shown[9] that structural analogies can be found between α-Al_2O_3 and γ-Al_2O_3 surfaces if one considers the speciation of surface OH extracted from the DFT work by Digne et al.[17] for γ-alumina and the theoretical[18−20] and experimental studies[21−26] on the surface structure of α-alumina C (0001), R $(1\bar{1}02)$, and A $(11\bar{2}0)$ planes. This analogy will be completed in this work by DFT modeling of the hydrated M $(10\bar{1}0)$ and A $(11\bar{2}0)$ surfaces that are not fully described in the literature.

α-Alumina-supported MoS_2 model catalysts have been prepared through equilibrium adsorption (selective adsorption)[27] in order to discriminate the reactivity of each alumina surface at the oxide/water interface. Subsequent sulfidation of each model catalyst was then realized at different temperatures to investigate the support effect in the genesis of the active phase (sulfidation rate, size of MoS_2 nanoparticles, and strength of metal−support interaction). The support effect is discussed in light of the speciation of hydroxyl groups on each surface orientation.

EXPERIMENTAL SECTION

Preparation of Model Oxide Catalysts (MoO_x/α-Al_2O_3). Prior to Mo deposition, 1 cm^2 α-alumina single crystals purchased from Mateck for the A $(11\bar{2}0)$, C (0001), and R $(1\bar{1}02)$ planes and from SurfaceNet for the M $(10\bar{1}0)$ orientation were washed with distilled water (30 min, 25 mL), HNO_3 (pH = 2, 30 min, 25 mL), NH_3 (pH = 9, 30 min, 25 mL), and again distilled water (30 min, 25 mL) before calcination in air in a muffle furnace overnight at 700 °C. Mo adsorption was then performed by equilibrating the α-Al_2O_3 wafers for 5 h in a heptamolybdate solution (10^{-9} < [Mo] < 10^{-2} M) obtained by dissolving $(NH_4)_6Mo_7O_{24}$, (Merck, >99% purity) in distilled water. The pH was not adjusted and was constant at 5.2.

The wafers were then rinsed twice (2 × 1 h) in distilled water (25 mL) and dried at room temperature in nitrogen flow. After drying, samples were calcined for 2 h at 450 °C in air in a muffle furnace.

Sulfidation of Model Oxide Catalysts (MoS_2/α-Al_2O_3). Sulfidation of the calcined MoO_x/α-Al_2O_3 model catalysts was carried out on samples with Mo loadings corresponding to the saturation coverage shown in Figure 1 (i.e., about 4 at. nm^{-2} for A $(11\bar{2}0)$ and M $(10\bar{1}0)$ planes and 1 at. nm^{-2} for the R $(1\bar{1}02)$ plane). Sulfidation was performed in a homemade glass reactor under a flow of 2 L/h of 15 mol % H_2S/H_2 at atmospheric pressure. Model catalysts were heated at 5 °C/min and kept at a constant temperature (100, 200, 300, 400,

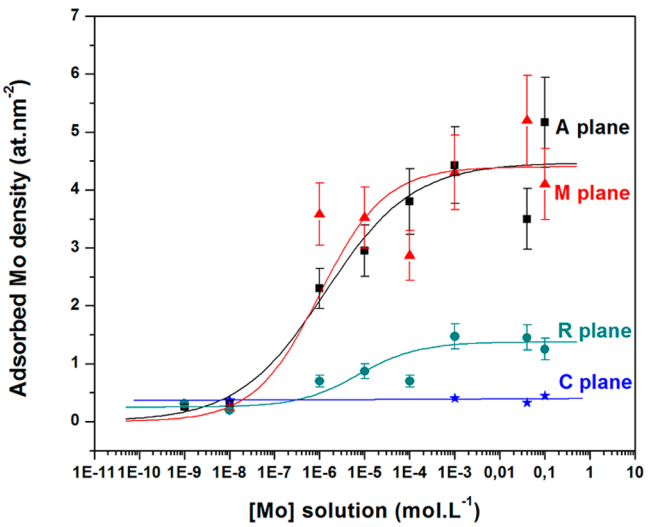

Figure 1. Surface molybdenum density determined by XPS as a function of molybdenum concentration for the A $(11\bar{2}0)$, C (0001), M $(10\bar{1}0)$, and R $(1\bar{1}02)$ α-Al_2O_3 planes. Each data point represents an average of a minimum of 3 independent experiments, and XPS measurements have been conducted after a calcination step (450 °C). Lines are drawn as a guide for clarity. Abscissa is in logarithmic scale.

DOI: 10.1021/jacs.5b10975
J. Am. Chem. Soc. 2015, 137, 15915−15928

or 450 °C) for 2 h. The reactor was then cooled down to 80 or 150 °C (depending on sulfidation temperature) for 1 h under argon (2 L/h) to remove any excess of sulfur. Catalysts were then kept under argon at room temperature before analysis. Such activation procedure corresponds to traditional gas-phase sulfidation conditions, usually applied in the literature to study supported HDT catalysts.

Characterization. *XPS.* For all model catalysts (oxide and sulfide forms), XPS spectra were recorded with an Omicron (ESCA+) instrument using a monochromatic Al X-ray source ($h\nu$ = 1486.6 eV) with an accelerating voltage of 14 kV and a current intensity of 20 mA (overall energy resolution was about 0.8 eV). Spectra were collected at a takeoff angle of 90° under a pressure lower than10^{-9} mbar at ambient temperature. For high-resolution spectra, the hemispherical analyzer operated at a pass energy of 20 eV and at 100 eV for the surveys. High-resolution scans with 0.1 eV steps were conducted over the following regions of interest: C 1s, O 1s, Al 2p, Mo 3d, and S 2p.

Binding energies (BEs) of the various elements were referenced to the Al 2p level of the alumina support at 74 eV. The collected spectra were analyzed by using the Casa XPS software package.[28] The spectral decomposition was performed by using Gaussian−Lorentzian functions after Shirley background subtraction.

For all oxide samples (i.e., MoO_x/α-Al_2O_3), the amount of deposited Mo was determined after calcination by integration of the Mo 3d XPS peak (sum of the $3d_{3/2}$ and $3d_{5/2}$ contributions) and Al 2p peak and with the following equation:[29]

$$[\mathrm{Mo(ads)}] = \frac{I_{\mathrm{Mo3d}} \cdot \sigma_{\mathrm{Al2p}} \cdot 2\rho_{\mathrm{Al2O3}}}{I_{\mathrm{Al2p}} \cdot \sigma_{\mathrm{Mo3d}} \cdot \mathrm{MW}_{\mathrm{Al2O3}}} \lambda_{\mathrm{Al2O3}}$$

With [Mo(ads)] the molybdenum surface concentration (at. nm^{-2}), I_{Mo3d} and I_{Al2p} the intensities of the corresponding XPS peaks, σ_{Al2p} and σ_{Mo3d} the photoionization cross sections (0.54 and 9.5 respectively), ρ_{Al2O3} (3.95 g cm^{-3}) and $\mathrm{MW}_{\mathrm{Al2O3}}$ (102 g moL^{-1}) are the density and molecular weight of α-alumina, and λ_{Al2O3} (31 Å) is the inelastic mean free path of Al 2p photoelectrons.

Sulfided samples were kept in the glass reactor under inert atmosphere before being rapidly transferred (less than 1 min) to the XPS analysis chamber. It was checked on selected samples transferred via a glovebox connected to the XPS instrument (without air exposure) that similar sulfidation ratio are obtained with or without air exposure providing a fast transfer (on the order of a minute). XPS spectra analyses were based on the methodology developed by Gandubert et al.[30] which takes into account the contributions of three different molybdenum oxidation states (i.e., Mo^{IV}, MoS_2; Mo^{V}, MoO_xS_y; and Mo^{VI}, MoO_3). The sulfidation rate (% MoS_2) was calculated by the following equation, using the peak area of each molybdenum species (A_{Mo}: sum of the $3d_{3/2}$ and $3d_{5/2}$ contributions):

$$\%\mathrm{MoS_2} = \frac{A_{\mathrm{Mo}}{}^{\mathrm{IV}}}{A_{\mathrm{Mo}}{}^{\mathrm{IV}} + A_{\mathrm{Mo}}{}^{\mathrm{V}} + A_{\mathrm{Mo}}{}^{\mathrm{VI}}}$$

TEM. Transmission electron microscopy (TEM) was used to determine the average length and stacking of the particles. Sampling of the MoS_2/α-Al_2O_3 model catalysts was based on a previous method developed for planar systems.[31] First, a drop of ethanol was deposited onto the model catalyst, and then the surface was scratched with a razor blade to concentrate the clusters of active phase into the solvent drop. The drop was then spread on a carbon-coated copper grid. TEM images were collected with a JEOL 2010 microscope operating at 200 kV. The average MoS_2 slab size and stacking were obtained by measuring at least 200−300 particles for each sample using *ImageJ 1.45* software.[32] The slab size was obtained by measuring the length of the MoS_2 fringes, and stacking was obtained by determining the number of fringes (layers) for one MoS_2 particle.

DFT Calculations. All calculations were performed using the ab initio plane-wave pseudopotential method as implemented in VASP (Vienna Ab Initio Simulation Package).[33,34] The generalized gradient approximation exchange-correlation functional of Perdew, Burke, and Ernzerhof PBE[35] was chosen to perform the periodic DFT calculations. In this approach, core electrons are not explicitly computed. Their interaction with the valence electrons is described by pseudopotentials from the projector augmented wave (PAW) approach,[36] while the valence electron wave functions are projected on a set of plane waves with a cutoff energy of 400 eV. The convergence criterion for the electronic self-consistent field relaxation was fixed to 10^{-5} eV. Geometry optimizations are performed using a conjugate-gradient algorithm, with a convergence criterion on forces of 0.02 eV $Å^{-1}$. Detailed construction of the A $(11\bar{2}0)$ and M $(10\bar{1}0)$ surfaces is included in the Supporting Information section. The surface energies have then been evaluated following the procedure described in ref 37 and explained in the Supporting Information section.

AFM. AFM images on model catalysts were recorded in air at room temperature on a commercial AFM (Nanoscope VIII Multimode AFM, Bruker Nano Inc., Nano Surfaces Division, Santa Barbara, CA) equipped with a 150 × 150 × 5 μm^3 scanner (J-scanner). The wafers substrates were fixed on a steel sample puck with adhesive. AFM analyses were performed using the peak force tapping mode (PFT), recently developed.[38] In this mode, the z-piezo is modulated far below the cantilever resonance frequency (2 kHz), with an amplitude around 110−120 nm, to obtain very fast approaching−retracting curves at each pixel of the image. Silicon tips on Si_3N_4 cantilevers were used (Bruker Nano Inc., Nano Surfaces Division, Santa Barbara, CA) with a spring constant of 0.4 N m^{-1}. Topographic images presented in this paper were flattened by a third order polynomial to correct surface tilt and eliminate bow effects (Nanoscope analysis software). To check for a potential oxidation of the sulfide phase during analysis, all MoS_2/α-Al_2O_3 samples were analyzed by XPS after AFM investigation. Sulfidation ratios obtained before and after AFM analysis are consistent showing that no significant oxidation occurs during AFM imaging.

X-ray Absorption. Characterization of planar model samples has been performed with GI-XAS (grazing-incidence X-ray absorption spectroscopy) in fluorescence mode with a Canberra 35 elements solid-state Ge detector at the Mo K edge (20 keV) on the SAMBA beamline at SOLEIL (Saint-Aubin, France).[39] Planar catalysts were fixed with carbon tape on a goniometer head. Characterization of reference compounds for Mo in octahedral coordination (ammonium heptamolybdate (AHM) and MoO_3) and tetrahedral coordination (Na_2MoO_4) was performed in transmission mode by diluting the sample in cellulose. Processing of the XAS data was carried out with the Demeter package.[40]

RESULTS AND DISCUSSION

1. Model Oxide Catalysts. The vast majority of HDT catalyst preparations at the industrial scale involve an aqueous-phase deposition of the precursor of the active phase (molybdenum oxoanions in the present case) on an oxide support (i.e., alumina). In these conditions, the speciation of the surface hydroxyl groups (i.e., Al−OH for aluminum oxides) is a key element for a molecular-scale understanding of active phase deposition since surface OH constitutes the adsorption sites for the metal to be deposited. In the present work, four different α-Al_2O_3 orientations (i.e., A $(11\bar{2}0)$, C (0001), M $(10\bar{1}0)$, and R $(1\bar{1}02)$ planes) were used to investigate the reactivity of different types of OH groups toward Mo adsorption. All adsorption experiments were performed at ambient temperature in aqueous solution, which implies that all α-alumina substrates are fully hydrated.

First, a quantitative evaluation of the adsorption capacity of each α-Al_2O_3 orientation was carried out by immersing the α-Al_2O_3 wafers in ammonium heptamolybdate solutions of various Mo concentrations from 10^{-1} to 10^{-9} M (natural pH value). Mo surface concentration was determined with XPS (based on the intensity of Mo 3d and Al 2p peaks) after rinsing the wafers with water and after a calcination step at 450 °C. This deposition procedure is denoted "equilibrium adsorption" or "selective adsorption" in the literature[27] since only

DOI: 10.1021/jacs.5b10975
J. Am. Chem. Soc. 2015, 137, 15915−15928

Table 1. Root Mean Square Surface Roughness (R_{rms}) from AFM Measurements of Planar MoO_x/α-Al_2O_3 Model Catalysts Calcined at 450 °C for 2 h with Various Surface Orientations[a]

	C plane	R plane	M plane	A plane
R_{rms} (nm) before Mo adsorption	0.10 ± 0.01	0.15 ± 0.01	0.13 ± 0.01	0.11 ± 0.01
R_{rms} (nm) after Mo adsorption and calcination	0.12 ± 0.01	0.22 ± 0.01	0.49 ± 0.01	0.54 ± 0.01

[a]Samples were prepared by selective Mo adsorption with a 4×10^{-2} M Mo solution. The root mean square surface roughness is expressed by the square root of the sum of the squares of the individual heights and depths from the mean line.

specifically adsorbed species will remain on the surface because the washing step removes loosely bound (nonadsorbed or physically adsorbed) species. The surface molybdenum density as a function of the molybdenum concentration is shown in Figure 1 for the various α-alumina orientations (each data point is the average of at least 3 independent experiments).

Figure 1 shows that, for all orientations, except for the C (0001) plane, there is an onset of Mo adsorption for a concentration of about 10^{-6} M and subsequently a saturation at about 10^{-3} M. However, the saturation in itself is highly dependent on the α-Al_2O_3 orientation. For both A ($11\bar{2}0$) and M ($10\bar{1}0$) planes, the Mo surface density reaches a maximum at about 4 at. nm^{-2}. This figure can be converted to a weight loading on a conventional powder γ-Al_2O_3 for comparison purposes: considering a specific surface area of 200 $m^2\ g^{-1}$ for γ-Al_2O_3, a surface density of 4 at. nm^{-2} corresponds to a weight loading of 16 wt % MoO_3.

On the R ($1\bar{1}02$) plane, the surface saturation is about 1 at. nm^{-2} (which can be converted to 4.6 wt % MoO_3/ γ-Al_2O_3), i.e., 4 times lower than for the A ($11\bar{2}0$) and M ($10\bar{1}0$) surfaces. The C (0001) plane is almost not reactive toward Mo adsorption at the pH of the experiments (pH = 5) since only less than 0.4 at. nm^{-2} were detected by XPS. The constant and negligible Mo adsorption in this latter case may be assigned to the presence of a weak fraction of reactive defects on the C (0001) surface.

These results underline the different Mo adsorption capacities for the various α-Al_2O_3 orientations. To sum up, three different behaviors can be drawn from these experiments: (i) a high surface reactivity (i.e., high Mo adsorption) for the A ($11\bar{2}0$) and M ($10\bar{1}0$) planes, (ii) a weak surface reactivity (i.e low Mo adsorption) for the R ($1\bar{1}02$) plane, and (iii) a negligible surface reactivity (i.e., almost no Mo adsorption) for the C (0001) plane.

These data can be compared to the results obtained on polycrystalline α-Al_2O_3 (specific surface area: 9 $m^2\ g^{-1}$, obtained by calcination at 1100 °C of commercial γ-Al_2O_3 extrudates). Mo adsorption was conducted in the same way as for planar substrates (i.e., equilibrium adsorption), and the surface concentration was determined with ICP-AES. For a Mo concentration of 10^{-2} M, a surface Mo concentration of 2 at. nm^{-2} was obtained which is significantly lower than the surface saturation on the A ($11\bar{2}0$) and M ($10\bar{1}0$) planes (4 at. nm^{-2}) and closer to that on the R ($1\bar{1}02$) plane (1 at. nm^{-2}). This result is in good agreement with the morphology of α-Al_2O_3 nanoparticles since it has been reported in the literature[18,41] that the C (0001) and R ($1\bar{1}02$) planes are the most predominant surfaces. Although A ($11\bar{2}0$) and M ($10\bar{1}0$) planes are more reactive toward Mo adsorption, their contribution to the total surface area is low, explaining a notably lower Mo surface density on polycrystalline α-Al_2O_3 than for planar A ($11\bar{2}0$) and M ($10\bar{1}0$) wafers.

The differences in reactivity among the various α-Al_2O_3 orientations are confirmed by AFM images (Table 1 and Supporting Information, Figure S1) obtained on model systems prepared with a Mo concentration of 4×10^{-2} M, i.e., with a Mo surface concentration corresponding to the adsorption saturation (Figure 1). First, it has to be noted that all orientations show an identically smooth surface before Mo adsorption (i.e., R_{rms} of 0.10−0.15 ± 0.01 nm, Table 1). This surface roughness barely changes for the C (0001) plane before and after Mo adsorption ($R_{rms} \sim 0.12$ nm), while for the R ($1\bar{1}02$) plane, the increase of surface roughness is more pronounced (from 0.15 nm for the bare surface to 0.22 nm after Mo adsorption) since many more molybdenum clusters of 2−8 nm (considering a spherical morphology for individual molybdenum oxide particles) homogeneously dispersed on the surface are discernible (Supporting Information, Figure S1). On A ($11\bar{2}0$) and M ($10\bar{1}0$) planes, a significant increase of surface roughness is observed up to 0.5 nm (Table 1) due to the presence of a high density of Mo oxide nanoparticles of larger size (2−15 nm) which are more or less aggregated. Hence, in line with the results of Mo adsorption, AFM images show that for the A ($11\bar{2}0$) and M ($10\bar{1}0$) orientations molybdenum oxide nanoclusters nearly cover the whole surface while for the R ($1\bar{1}02$) plane these species are more spread on the surface and almost absent for the C (0001) plane.

A molecular-scale investigation of Mo speciation on the model catalysts prepared on the A ($11\bar{2}0$) and M ($10\bar{1}0$) planes after calcination was carried out with grazing-incidence X-ray absorption spectroscopy (GI-XAS). Detection of a small amount of adsorbates on planar model systems is facilitated in grazing-incidence geometry due to an enhancement of the fluorescence intensity in total reflection conditions.[42] Nevertheless, due to the low Mo content, only the XANES part of the absorption spectrum at the Mo K-edge of the most concentrated samples (A ($11\bar{2}0$) and M ($10\bar{1}0$) planes) was exploitable and collected. First, spectra of Mo reference compounds where Mo adopts a 6-fold coordination (ammonium heptamolybdate (noted AHM) and molybdenum trioxide (MoO_3)) or a 4-fold coordination (sodium molybdate, Na_2MoO_4) were recorded as XANES fingerprints (Figure 2) since it is well-known[43] that the pre-edge region (i.e., 1s to 4d transition at 20 000−20 010 eV) shows a distinct signature for octahedral and tetrahedral coordination. The corresponding 1s to 4d transition is dipole-forbidden for centrosymmetric (octahedral) environments and will show a weak intensity while for tetrahedral geometry the pre-edge transition will become partially dipole allowed (and consequently more intense) through mixing between Mo 4d and 5p orbitals. Such a difference is clearly seen in Figure 2 where the pre-edge region for Na_2MoO_4 is visibly more intense than that for AHM or MoO_3.

The pre-edge feature of the model catalysts obtained for Mo concentration of 4×10^{-2} M corresponding to the Mo saturation is clearly similar to the reference compounds with octahedral Mo coordination, and a tetrahedral symmetry can be excluded for supported Mo nanoclusters. Comparison of the

DOI: 10.1021/jacs.5b10975
J. Am. Chem. Soc. 2015, 137, 15915−15928

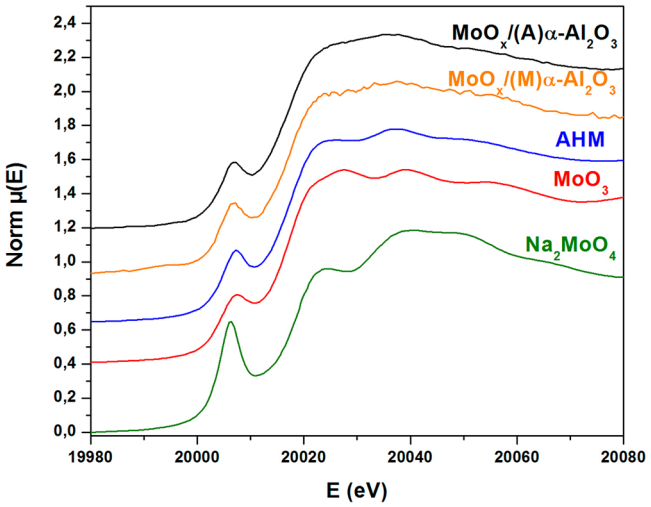

Figure 2. Mo K-edge XANES spectra of reference compounds and model Mo catalysts supported on the A $(11\bar{2}0)$ and M $(10\bar{1}0)$ orientations of α-Al_2O_3. Samples were prepared by selective Mo adsorption with a 4×10^{-2} M Mo solution. (Norm $\mu(E)$: normalized absorption.)

edge region (above 20010 eV) confirms that the model systems show similar features with respect to polyoxo 6-fold-coordinated molybdenum compounds (i.e., AHM and MoO_3).

However, a detailed analysis of the XANES spectra reveals some differences. More precisely, AHM and the model catalysts present three successive maxima at about 20 023, 20 037, and 20 053 eV whereas for MoO_3 the same three features are shifted to slightly higher energy (20 027, 20 039, and 20 057 eV). It is also noticeable that the relative intensity of the three maxima for AHM and the model catalysts are comparable with a maximum intensity for the second feature at about 20 037 eV. Conversely, for MoO_3 the first and the second maxima have similar relative intensity.

Tougerti et al.[43] have recently applied multiple scattering (MS) simulation of the XANES region for various polyoxomolybdate compounds in order to apprehend more precisely the origin of these different features. In fact, there are several nonequivalent Mo positions in polyxomolybdates, and each of these positions has a direct and distinct impact on the relative intensity of the different maxima observed at the edge. Therefore, Tougerti et al.[43] demonstrated that the XANES region can be used as very sensitive spectral fingerprint for closely related polyoxomolybdates. Figure 2 shows that the XANES regions for Mo supported on A $(11\bar{2}0)$ and M $(10\bar{1}0)$ α-Al_2O_3 orientations are fully comparable both in terms of position and intensity, despite a lower signal-to-noise ratio for the M $(10\bar{1}0)$ plane.

It can thus be concluded that molybdenum speciation is similar on A $(11\bar{2}0)$ and M $(10\bar{1}0)$ planes, in line with a comparable reactivity of those two orientations as shown in Figure 1. Moreover, the XANES features are also highly similar to those shown by AHM (with higher resolution for the latter) while MoO_3 shows a distinct spectrum with identical relative intensity for the first and second maxima. Hence, it can be concluded that Mo nanoclusters formed on the A $(11\bar{2}0)$ and M $(10\bar{1}0)$ orientations are structurally related to AHM (with edge-shared octahedra) albeit with a lower organization explaining the broader and less defined peaks in the XANES region.

2. Surface Hydroxyl Groups. Rationalization of the individual reactivity of each α-Al_2O_3 orientation requires a comprehensive description of the various surface hydroxyl groups on all alumina planes. As mentioned before, the surface structures of the C (0001) and R $(1\bar{1}02)$ planes have been extensively studied (both theoretically and experimentally) in the presence of water in the literature.[9,19] For the C (0001) plane, experimental and theoretical data show that the surface is terminated with bridging oxygen atoms bound to two aluminum atoms in octahedral symmetry (i.e., Al_{6c}-μ_2-OH). As for the R $(1\bar{1}02)$ plane, the situation is less straightforward since different surface OH groups have been considered (i.e., Al_{6c}-μ_n-OH with n = 1, 2, or 3 or Al_{4c}-μ_1-OH) and there is no consensus up to now with three distinct proposed models (see Bara et al.[9] for a review). The surface structure of the two other orientations A $(11\bar{2}0)$ and M $(10\bar{1}0)$ have only been scarcely described. High-resolution specular X-ray reflectivity on the A $(11\bar{2}0)$ plane[26] suggests the existence of Al_{6c}-μ_n-OH groups with n = 1, 2, or 3, but no data have been reported on the surface OH speciation on the M $(10\bar{1}0)$ plane to the best of our knowledge.

Therefore, in order to gain a deeper insight into the surface structure of the different Al_2O_3 orientations, the hydration of the A $(11\bar{2}0)$ and M $(10\bar{1}0)$ surfaces has been studied theoretically in this work by DFT calculations. The dehydrated surfaces were obtained by cleaving the α-alumina bulk model (experimental hexagonal unit cell with a = 4.76 Å and c = 12.99 Å)[44] along the (110) and (100) crystallographic directions, respectively (see Experimental Section and Supporting Information, Figure S2). In order to take into account the fact that molybdenum adsorption experiments were conducted in aqueous solutions, only fully hydrated surfaces were considered, and the water partial pressure was chosen equal to 1 atm in the thermodynamic calculations. Our goal was not to perform a full study of the surface hydration (beyond the scope of the present paper) but to obtain a realistic surface termination of the hydrated A $(11\bar{2}0)$ and M $(10\bar{1}0)$ surfaces. The maximum hydroxyl coverage is obtained once all surface aluminum atoms recover an octahedral coordination similar to their coordination in the bulk of α-alumina. Additional water molecules could only be added to the surface through hydrogen bonding with the surface hydroxyl groups.

The maximum hydroxyl coverage is found to be 19 OH nm^{-2} for the M $(10\bar{1}0)$ termination (6 water molecules per elementary cell) and 17 OH nm^{-2} for the A $(11\bar{2}0)$ termination (3 water molecules per elementary cell, or 9 in the simulation box). Table 2 gives the surface energies calculated for the dehydrated and hydrated M $(10\bar{1}0)$ and A $(11\bar{2}0)$ surfaces at room temperature (at which adsorption experiments are performed) and at 100 °C (water boiling point). The hydration of the surface strongly stabilizes the surfaces, and the A $(11\bar{2}0)$

Table 2. DFT-Calculated Surface Energies for the Dehydrated and Fully Hydrated A $(11\bar{2}0)$ and M $(10\bar{1}0)$ Facets of α-Alumina

		θ (OH nm^{-2})	Γ at RT (mJ m^{-2})	Γ at 100 °C (mJ m^{-2})
M $(10\bar{1}0)$ plane	dehydrated	0.0	2020	2020
	hydrated	19	554	790
A $(11\bar{2}0)$ plane	dehydrated	0.0	1870	1870
	hydrated	17	460	660

DOI: 10.1021/jacs.5b10975
J. Am. Chem. Soc. 2015, 137, 15915−15928

surface appears slightly more stable than the M $(10\bar{1}0)$ surface, although their surface energies are rather close. The surface energies of both surfaces are in the range 400−800 mJ m^{-2} which are in the range of boehmite γ-AlOOH surface energies in water (from 465 to 825 mJ m^{-2}),[45] indicating that the hydrated α-alumina surface models presented in this work are representative of water/alumina interfaces.

Figure 3 shows the most stable surface structure for the hydrated M $(10\bar{1}0)$ surface (19 OH nm^{-2}). The aluminum

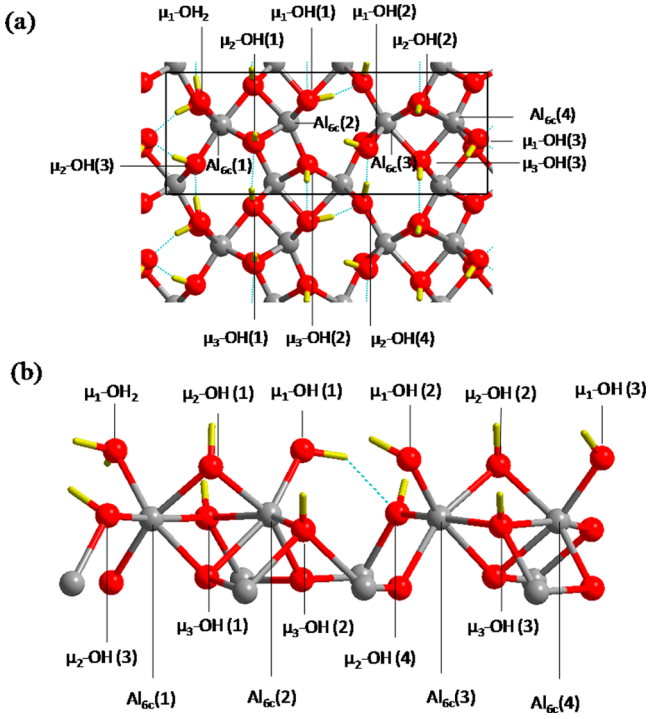

Figure 3. DFT-optimized surface structure of the fully hydrated M $(10\bar{1}0)$ surface (19 OH nm^{-2}) of α-alumina: (a) top view and (b) side view. The box delimits the simulation box. Gray: aluminum atom. Red: oxygen atom. Yellow: hydrogen atom.

atoms that were tetracoordinated in the dehydrated state (Al_{4c}, see Supporting Information) are hexacoordinated (Al_{6c}) after hydration since the two oxygen vacancies per aluminum atom are filled by coordination of two hydroxyl fragments. Although the elementary cell contains four aluminum atoms, and thus eight potential vacancies, two water molecules can be adsorbed by bridging two aluminum atoms ($Al_{4c}(1)/Al_{4c}(2)$ and $Al_{4c}(3)/Al_{4c}(4)$), so that only six water molecules at most can be adsorbed by this surface. Water mainly dissociates on the surface to form OH^- and H^+ moieties, and various kinds of hydroxyl groups result from this dissociative adsorption and are distributed as follows (for a detailed description see Supporting Information): 30% (33%) of Al_{6c}-μ_1-OH, 40% (33%) of Al_{6c}-μ_2-OH, 30% (33%) of Al_{6c}-μ_3-OH.

Water is also adsorbed associatively on this surface (see μ_1-OH_2 on $Al_{6c}(1)$). Alternatively, this water molecule can dissociate into one μ_1-OH and one μ_3-OH, with this form being slightly less favorable (less than 5 kJ mol^{-1}). Numbers in brackets above correspond to this latter case.

Figure 4 shows the most stable surface structure for the hydrated A $(11\bar{2}0)$ surface (17 OH nm^{-2}). In this case, the aluminum atoms are originally pentacoordinated (Al_{5c}), and thus have only one vacancy per aluminum atom that can be

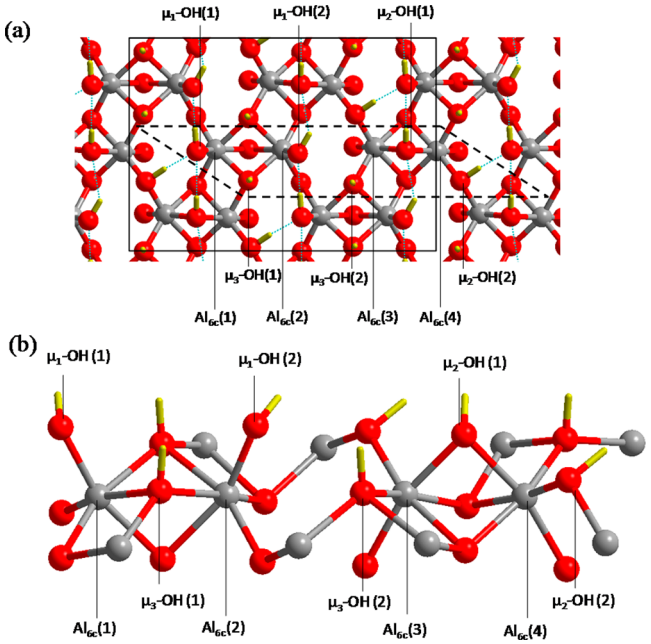

Figure 4. DFT-optimized surface structure of the fully hydrated A $(11\bar{2}0)$ surface (17 OH nm^{-2}) of α-alumina: (a) top view, (b) side view. The plain box delimits the simulation box and the dotted box the surface elementary cell. Gray: aluminum atom. Red: oxygen atom. Yellow: hydrogen atom.

filled by a hydroxyl fragment in order to recover an octahedral geometry. However, similarly to the M $(10\bar{1}0)$ surface, one hydroxyl fragment can bridge two aluminum atoms ($Al_{4c}(3)/Al_{4c}(4)$), and thus only 3 water molecules per elementary cell can be accommodated by this surface. For the most stable optimized surface structure, the following distribution of hydroxyl groups is obtained (see Supporting Information for a detailed description): 33% of Al_{6c}-μ_1-OH, 33% of Al_{6c}-μ_2-OH, 33% of Al_{6c}-μ_3-OH.

This optimized structure and hydroxyl types distribution are in good agreement with the recent proposal by Catalano et al.[26]

DFT calculations of hydrated A $(11\bar{2}0)$ and M $(10\bar{1}0)$ surfaces reveal that both orientations have a similar speciation of surface OH groups which is in good agreement with their close reactivity toward Mo adsorption (Figure 1). Both surfaces indeed contain surface octahedral aluminum atoms only and exhibit a combination of μ_1-OH and bridging μ_2-OH and μ_3-OH surface groups. The detailed description of surface OH speciation on the various α-alumina orientations can then be used to analyze the surface charge of the different planes which can be seen as a decisive descriptor for explaining the Mo sorption dissimilarities observed in Figure 1.

3. Role of Hydroxyl Groups toward Adsorption: PZC.

The adsorption mode of Mo polyoxoanion at the oxide/water interface is considered to be mainly electrostatic.[46−48] Hence, starting from a polymeric anionic Mo precursor (heptamolybdate anion), metal adsorption will be favored on a positively charged surface, i.e., below the point of zero charge (PZC). Therefore, a rational understanding of Mo adsorption requires a comprehensive knowledge of the surface charge and PZC of the various surface planes investigated in the present work.

It is important to mention that the following discussion is restricted to the surface charge developed in the plane of the surface hydroxyl group (i.e., the surface potential) and consequently to the PZC which corresponds to a zero net

DOI: 10.1021/jacs.5b10975
J. Am. Chem. Soc. 2015, 137, 15915−15928

surface charge (i.e., an equal number of positively and negatively charged surface OH sites). Therefore, we leave aside all considerations on the zeta potential (and isoelectric point, IEP which is the pH where the zeta potential is zero) which is defined as the electrical potential at the shear plane (i.e., at some distance from the surface) determined, for example, by streaming potential. As a matter of fact, a long-lasting and unresolved debate exists on the discrepancy between PZC and IEP values for planar alumina wafers,[49,50] but this discussion is beyond the scope of this work.

Determination of the surface charge and the associated PZC can derive from the MUSIC model[51] considering the pK_a of the various surface hydroxyl groups associated with the experimental and/or theoretical surface structure models for the various α-Al_2O_3 orientations.[52] Validation of this approach can also be obtained with SFG spectroscopy[53] since this technique yields vibrational spectra in the OH region (surface hydroxyls and interfacial water) that will be highly dependent on the surface potential imposed by protonation/deprotonation of surface hydroxyls.[49]

The surface charge of the C (0001) plane at the oxide/water interface will first be considered since this surface has been extensively studied in the literature. It has been demonstrated that the surface is terminated by doubly coordinated oxygen atoms bound to octahedral aluminum atoms only.[20,21,54] The MUSIC model predicts that this type of surface group (Al_{6c}-μ_2-OH) will have a low protonation and high deprotonation pK_a (0 and 11.9, respectively) meaning that doubly coordinated OH should be neutral over a large pH range,[49,51,55] and a more or less zero electrostatic surface potential is predicted between pH 3 and 9.[50] This situation is schematically represented on Scheme 1. SFG data are in good agreement with the MUSIC model since the amplitude of the "ice-like" water band of the SFG spectra (i.e., dependent on the surface potential) is minimal and consequently confirms a minimal surface potential between pH 4 and 8.[50,53] A resulting PZC of 6.3 can be extracted from SFG data[53] which is also in good agreement with half the sum of the pK_a.

Scheme 1. Schematic View of the Surface Charge for the C (0001), R (1$\bar{1}$02), A (11$\bar{2}$0), and M (10$\bar{1}$0) Planes as a Function of pH[a]

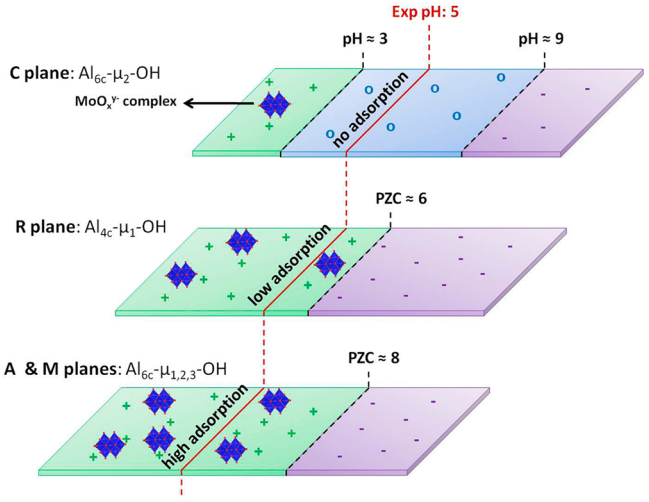

[a]See text for a discussion on the PZC for each surface orientation. Red line indicates the experimental pH used for equilibrium adsorption of Mo. Blue polyhedra are a schematic representation of the adsorption of Mo polyoxoanion.

The situation for the R (1$\bar{1}$02) plane is less straightforward since several surface models have been proposed in the literature. A detailed discussion is available in the work of Tougerti et al.,[19] but the main points are summarized hereafter. The surface structure proposed by Trainor et al.[22] involves three types of hydroxyl groups, Al_{6c}-μ_1-OH, Al_{6c}-μ_2-OH, and Al_{6c}-μ_3-OH, while Catalano et al.[25] suggested an alternative surface termination with the absence of doubly coordinated OH. However, this second proposal should result in an identical surface charging behavior since it was shown above that Al_{6c}-μ_2-OH species are neutral over a large pH range implying that only mono- and tricoordinated OH groups contribute to the surface charge. On the basis of surface acidity constants determined by the MUSIC model[51,55−57] (Al_{6c}-μ_1-$OH_2^{0,5+}$, pK_a = 9.9; Al_{6c}-μ_3-$OH^{0,5+}$, pK_a = 5.9), a PZC of about 8 can be predicted for the R (1$\bar{1}$02) plane (half the sum of the two pK_a's) considering that the surface is terminated by an equal number of both types of surface functional groups (Table 3).[50,52]

However, a lower PZC of 6.7 was deduced from SFG data.[58] Moreover, Tougerti et al.[19] proposed an alternative R (1$\bar{1}$02) surface structure based on ab initio calculations. In this latter case, only singly coordinated surface OH species on tetrahedral aluminum atoms (Al_{4c}-μ_1-OH, Table 3) are present on the surface with different surface acidity constants depending on the authors: the MUSIC model[55] predicts a pK_a of 5 while Contescu et al.[59] proposed a pK_a of 6.7. Hence, a PZC of 5.5 or 7.2, respectively,[19] can be deduced from these pK_a's which is in the range of the experimental PZC obtained from SFG (i.e., 6.7)[58] and that deduced from the adsorption isotherm of ammonium heptamolybdate (i.e., about 5.5−6).[19]

There is clearly a slight variation of PZC values among the different sources, but all data extracted from SFG, the MUSIC model applied to Al_{4c}-μ_1-OH surface sites, and Mo adsorption isotherm converge to an average PZC of about 6 for the R (1$\bar{1}$02) plane (Scheme 1). This figure is significantly lower than that deduced from the surface structures of Trainor et al.[22] and Catalano et al.[25] for an R (1$\bar{1}$02) plane terminated with 6-fold coordinated aluminum atoms.

DFT calculations reported above for fully hydrated A (11$\bar{2}$0) and M (10$\bar{1}$0) orientations have shown that both planes expose singly, doubly, and triply coordinated OH groups bound to octahedral aluminum atoms. The surface density of each surface species is reported in Table 3 which shows that there is an identical number of singly and triply coordinated surface OH groups for both A (11$\bar{2}$0) and M (10$\bar{1}$0) planes. As discussed above for the R (1$\bar{1}$02) plane considering the termination favored by Catalano et al.,[22] the MUSIC model predicts a PZC of about 8 for a surface terminated by an equal number of Al_{6c}-μ_1-OH and Al_{6c}-μ_3-OH surface groups.[50,52] SFG data on the A (11$\bar{2}$0) plane[60] suggests a lower PZC (i.e., 6.7) that is identical to that determined for the R (1$\bar{1}$02) plane. However, SFG data for the A (11$\bar{2}$0) plane are less conclusive since the evolution of the amplitude of the two bands assigned to interfacial water molecules (3180 and 3450 cm^{-1}) is not parallel while an identical response toward the surface charge would be expected.

Hence, the MUSIC-derived PZC for the A (11$\bar{2}$0) plane will be considered as a more reliable value in this case (Scheme 1). No spectroscopic data are available for the M (10$\bar{1}$0) plane to the best of our knowledge, but with the close structural

DOI: 10.1021/jacs.5b10975
J. Am. Chem. Soc. 2015, 137, 15915−15928

Table 3. Quantification of the Different Surface Hydroxyl Groups for the A (11$\bar{2}$0) and M (10$\bar{1}$0) Planes Based on DFT Calculations Reported in This Work and For the R (1$\bar{1}$02) Plane, Quantification is Based on the Theoretical Work of Tougerti et al.[19] and on the Experimental Work of Catalano et al.[25a]

	OH surface density (at. nm^{-2})			
	R facet Catalano termination	R facet Tougerti termination	A facet	M facet
Al_{4c}-μ_1-OH	0	8	0	0
Al_{6c}-μ_1-OH	8	0	5.6	4.9 (6.5)
Al_{6c}-μ_2-OH	0	0	5.6	6.5 (6.5)
Al_{6c}-μ_3-OH	8	0	5.6	4.9 (6.5)

[a]For the M (10$\bar{1}$0) plane, the figures in brackets are related to the nearly isoenergetic surface model in which the water molecule is dissociated into one μ_1-OH group and one μ_3-OH group.

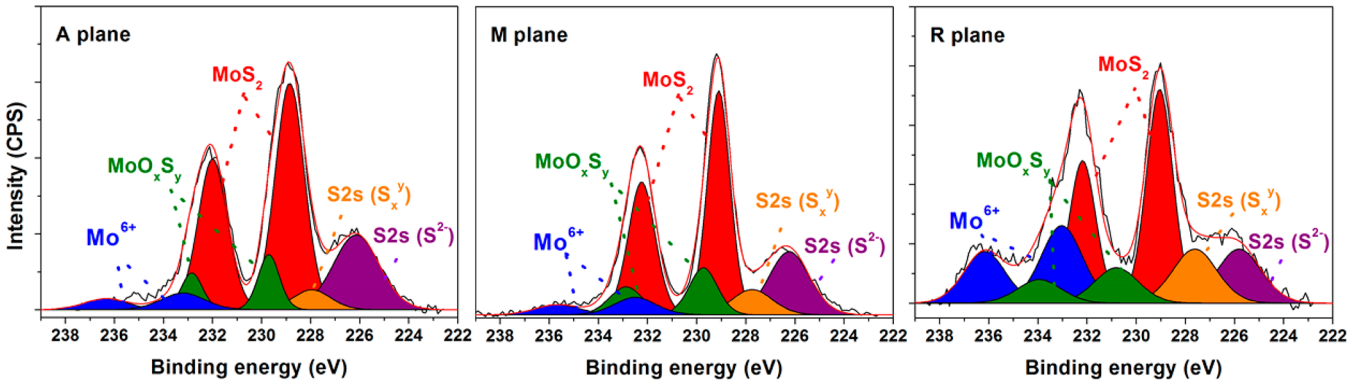

Figure 5. Decomposition of Mo_{3d} and S_{2s} XPS peaks for model catalysts sulfided at 450 °C for 2 h, supported on A (11$\bar{2}$0), M (10$\bar{1}$0), and R (1$\bar{1}$02) α-alumina single crystal substrates.

similarity between the A (11$\bar{2}$0) and M (10$\bar{1}$0) plane, an identical PZC will be considered for both orientations.

The different PZC determined for each α-Al_2O_3 surface orientations can explain the individual reactivity of each surface (Figure 1). At the natural pH of the Mo solution (i.e., pH 5), A (11$\bar{2}$0) and M (10$\bar{1}$0) planes are more positively charged (PZC ≈ 8) and thus adsorb more Mo oxoanions as compared to the R (1$\bar{1}$02) plane (PZC around 6). As for the C (0001) plane, bicoordinated OH should be neutral and, thus, unreactive toward metal adsorption in a large pH range. The inertness of the basal C(0001) plane is in line with several studies devoted to the adsorption of different cations in the aqueous phase on this surface.

For example, Bargar et al.[61,62] have shown that Al_{6c}-μ_2-OH sites favor only a weak outer sphere adsorption of Pb^{II} via hydrogen bonding. Similarly, no Ni^{II} uptake on the C (0001) plane has been found after adsorption of nickel-ethylenediamine complex at neutral pH.[63] Thus, differences in the surface electrostatic behavior among different planes can well explain the higher reactivity toward Mo adsorption of A (11$\bar{2}$0) and M (10$\bar{1}$0) orientations as depicted in Scheme 1.

It has also to be emphasized that the surface OH density on each plane is in agreement with the individual surface reactivity toward Mo adsorption. Taking into account the surface density of reactive surface OH (i.e., leaving aside neutral Al_{6c}-μ_2-OH), A (11$\bar{2}$0) and M (10$\bar{1}$0) planes exhibit a higher surface OH density (11 and 10 OH nm^{-2}, respectively) than for the R (1$\bar{1}$02) plane (8 OH nm^{-2}). Hence, the higher Mo adsorption on the A (11$\bar{2}$0) and M (10$\bar{1}$0) surfaces is explained both by the higher density of anchoring sites (surface OH) and by their higher protonation degree due to a high PZC.

It has been shown above that the individual reactivity of specific surface OH groups involved during metal complex adsorption can be studied through the use of planar model catalysts. Next, the sulfidation of the same model catalysts has been performed in order to investigate the role of the oxide support toward the structure of the catalytically active sulfide phase.

4. Influence of the Support on Sulfidation. Sulfidation of the calcined model catalysts was performed in the gas phase (15% H_2S/H_2) at different temperatures from 100 to 450 °C for A (11$\bar{2}$0), M (10$\bar{1}$0) and R (1$\bar{1}$02) orientations. Supported Mo catalysts on the C (0001) plane were not sulfided since the amount of adsorbed molybdenum was found to be negligible (Figure 1). As for the A (11$\bar{2}$0), M (10$\bar{1}$0), and R (1$\bar{1}$02) planes, sulfidation was conducted on samples prepared with a 4×10^{-2} M Mo solution, corresponding to the adsorption saturation found in Figure 1: about 4 at. nm^{-2} for the A (11$\bar{2}$0) and M (10$\bar{1}$0) planes and 1 at. nm^{-2} for the R (1$\bar{1}$02) plane. Activated model systems were analyzed by XPS, and decomposition of Mo_{3d}, S_{2s}, and S_{2p} peaks was carried out following the comprehensive work of Gandubert et al.[64] considering that molybdenum can be present in three different species: (i) molybdenum oxide (MoO_3), (ii) molybdenum oxysulfide species (MoO_xS_y), and (iii) molybdenum disulfide (MoS_2).

As an example, Figure 5 shows the decomposition of the XPS spectra for model catalysts sulfided at 450 °C (see Supporting Information for S 2p decomposition, Figure S3). The binding energies (BEs) of Mo $3d_{5/2}$ and S $2p_{3/2}$ contributions as well as the relative intensities (%) of the different molybdenum and sulfur species are reported in Tables 4 and 5.

Mo $3d_{5/2}$ contributions at 229, 230, and 233 eV are assigned to molybdenum disulfide, molybdenum oxysulfide, and molybdenum oxide, respectively, in good agreement with literature data.[64] The S 2p signal is made of two different

DOI: 10.1021/jacs.5b10975
J. Am. Chem. Soc. 2015, 137, 15915−15928

Table 4. Binding Energies (eV) and Relative Contribution (%) of the Mo $3d_{5/2}$ Peak Measured by XPS for Model Catalysts Supported on A ($11\bar{2}0$), M ($10\bar{1}0$), and R ($1\bar{1}02$) Planes and Sulfided at 450 °C

	MoS_2		MoO_xS_y		MoO_3	
	BE (eV)	%	BE (eV)	%	BE (eV)	%
MoS_2/(A) α-Al_2O_3	228.9	78	229.7	13	233.2	9
MoS_2/(M) α-Al_2O_3	229.1	87	230.1	8	233.2	5
MoS_2/(R) α-Al_2O_3	229.0	60	230.8	7	233.0	33

Table 5. Binding Energies (eV) and Relative Contribution (%) of the S $2p_{3/2}$ Peak Measured by XPS for Model Catalysts Supported on A ($11\bar{2}0$), M ($10\bar{1}0$), and R ($1\bar{1}02$) Planes and Sulfided at 450 °C

	S^{2-}		S_x^y	
	BE (eV)	%	BE (eV)	%
MoS_2/(A) α-Al_2O_3	161.9	82	163.7	18
MoS_2/(M) α-Al_2O_3	162.0	87	163.7	13
MoS_2/(R) α-Al_2O_3	162.0	57	163.8	43

contributions (that are also visible on the S 2s photopeak). The low binding energy peak (162 ± 0.1 eV) is assigned to S^{2-} species involved in the MoS_2 sulfide phase.[65] The second peak at higher binding energy (163.7 ± 0.1 eV) has been assigned to various species in the literature: oxysulfide compounds,[65] S_2^{2-} bridging ligands,[66,67] or SH species.[68−70] It is thus denoted as S_x^y in Table 5.

The main difference among each surface orientation at 450 °C arises from the relative contribution of the molybdenum sulfide phase (i.e., sulfidation ratio from the Mo 3d or S 2p contributions) which is much more important for the A ($11\bar{2}0$) and M ($10\bar{1}0$) orientations with respect to the R ($1\bar{1}02$) plane (Table 4). Conversely, the oxysulfide (MoO_xS_y) contribution is minimal and similar for all model catalysts.

XPS analysis was then conducted on the model systems after sulfidation at different temperatures in order to follow the evolution of the sulfidation ratio on each surface orientation (Figure 6). As expected, the MoS_2 ratio increases with an increase in the sulfidation temperature. The relative contribution of MoS_2 is distinctly higher for A ($11\bar{2}0$) and M ($10\bar{1}0$) orientations as compared to the R ($1\bar{1}02$) plane which shows that there is a clear surface-dependence of the sulfidation ratio.

Dispersion of molybdenum species based on the Mo 3d to Al 2p ratio from XPS has also been followed with temperature in order to check for a potential aggregation of molybdenum particles (Figure 7). It is shown that the Mo dispersion remains constant over all the temperature range for the three different surfaces. A slight decrease is only observed at 450 °C for the A ($11\bar{2}0$) and R ($1\bar{1}02$) planes, but it does not indicate a significant change in molybdenum dispersion on the surface. These results point out that no aggregation takes place during sulfidation whatever the surface and temperature considered. Hence, the differences observed in the evolution of the sulfidation ratio with temperature for the different surfaces (Figure 6) cannot be due to sintering of Mo particles.

AFM images of sulfided samples show homogeneously dispersed nanoparticles of active phase for the three facets (Figure 8). However, the density of Mo particles is noticeably higher on A ($11\bar{2}0$) and M ($10\bar{1}0$) orientations as compared to the R ($1\bar{1}02$) plane in agreement with the adsorption capacity of each facet (Figure 1). This observation is also confirmed by

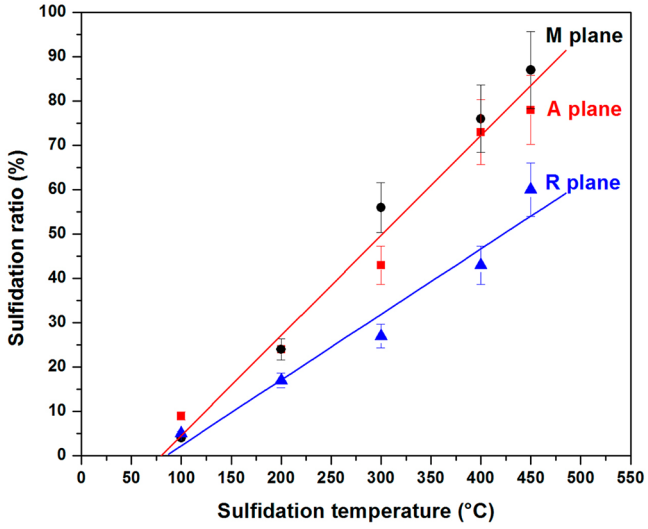

Figure 6. Sulfidation ratio for model catalysts supported on A ($11\bar{2}0$), M ($10\bar{1}0$), and R ($1\bar{1}02$) α- alumina single crystals as a function of sulfidation temperature. Samples were prepared by selective Mo adsorption with a 4×10^{-2} M Mo solution. The red straight line is a linear regression through the A and M data and the blue line through the R data.

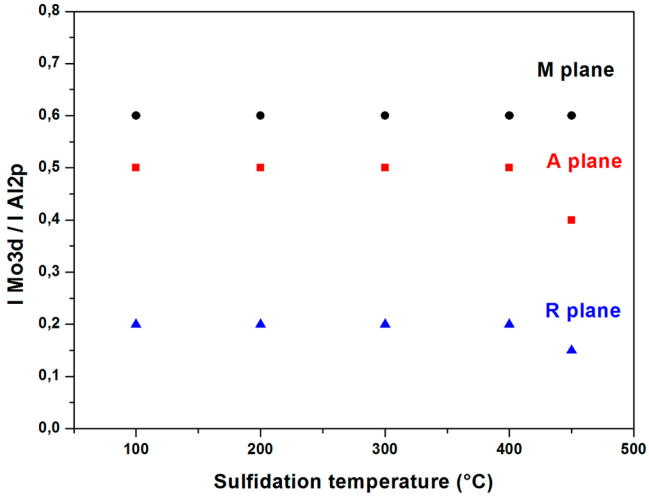

Figure 7. Dispersion (I(Mo 3d)/I(Al 2p) from XPS) of model catalysts supported on A ($11\bar{2}0$), M ($10\bar{1}0$), and R ($1\bar{1}02$) α-alumina single crystals as a function of sulfidation temperature. Samples were prepared by adsorption of a 4×10^{-2} M Mo solution, calcination at 450 °C, and sulfidation.

examining the cross section (white line in Figure 8) that shows a similar particle density on A ($11\bar{2}0$) and M ($10\bar{1}0$) planes and a lower density on the R ($1\bar{1}02$) plane. Likewise, surface roughness is higher for A ($11\bar{2}0$) and M ($10\bar{1}0$) orientations (0.54 and 0.49 nm, respectively) as compared to the R ($1\bar{1}02$) facet (0.33 nm). A slight difference is also observed for the height of the Mo particles with a higher average height for A ($11\bar{2}0$) and M ($10\bar{1}0$) surfaces (1.5−2 nm) with respect to the R ($1\bar{1}02$) plane (0.5−1 nm). A higher stacking of MoS_2 slabs for A ($11\bar{2}0$) and M ($10\bar{1}0$) surfaces could explain this difference and will be discussed later, with TEM analysis.

An evaluation of MoS_2 slab size has also been performed using the Gwyddion software[71] considering a round shape for all particles. An average diameter around 5.3 nm is found for

DOI: 10.1021/jacs.5b10975
J. Am. Chem. Soc. 2015, 137, 15915−15928

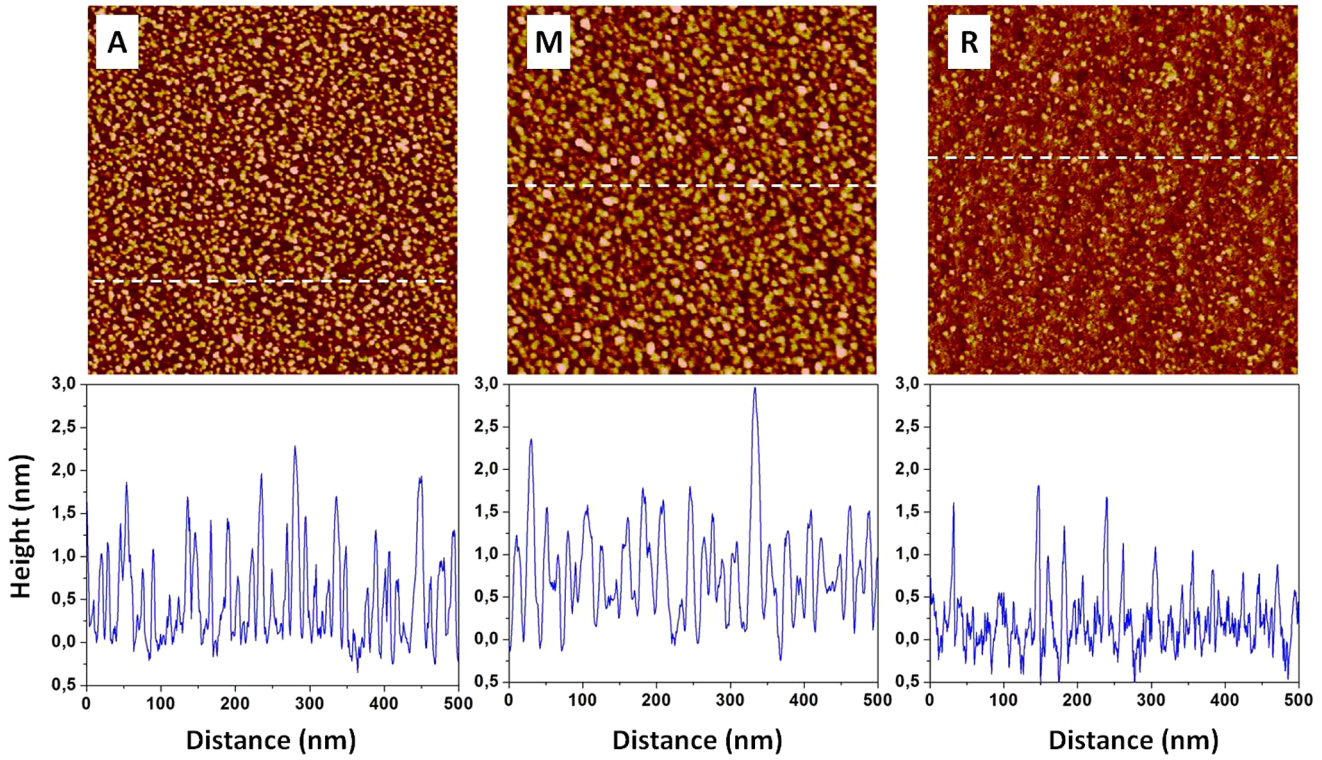

Figure 8. Representative AFM images (500 × 500 nm^2, peak force tapping mode in air, z-scale 3.5 nm) recorded on sulfided Mo catalysts supported on A (11$\bar{2}$0), M (10$\bar{1}$0), and R (1$\bar{1}$02) α-alumina single crystals. Samples were prepared by a selective adsorption of a 4 × 10^{-2} M Mo solution, calcination at 450 °C, and sulfidation at 450 °C for 2 h. Cross sections were taken at the position indicated by the white dashed lines on the images.

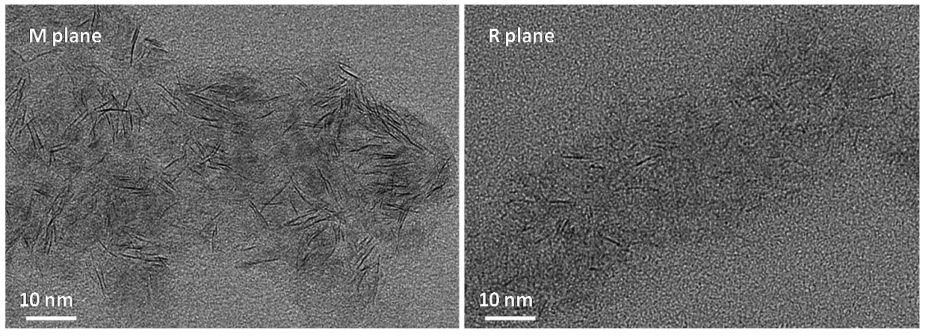

Figure 9. Typical TEM images of model catalysts supported on M (10$\bar{1}$0) and R (1$\bar{1}$02) facets sulfided at 450 °C in H_2S/H_2.

A (11$\bar{2}$0) and M (10$\bar{1}$0) surfaces while a lower diameter of 3.4 nm is obtained for the R (1$\bar{1}$02) plane. However, due to limited resolution, AFM images do not reveal significant dissimilarities in MoS_2 morphology (i.e., triangular to hexagonal shape)[72] among the three oxide support facets.

In order to confirm a support effect on the slab size and stacking suggested by AFM, TEM was used for model catalysts activated at the highest sulfidation temperature (450 °C). Typical TEM images of supported MoS_2 nanostructures[73] are shown in Figure 9 where MoS_2 slabs are visible in side projection (parallel to the electron beam). A higher density of MoS_2 particles is visible for the M (10$\bar{1}$0) plane with respect to the R (1$\bar{1}$02) plane in line with AFM results.

Size distributions determined from the corresponding TEM images are presented in Figure 10. The distribution is distinctly shifted toward smaller particles for the R (1$\bar{1}$02) plane. The average size of MoS_2 slabs supported on the R (1$\bar{1}$02) plane is 2.8 ± 0.1 nm whereas the mean size on A (11$\bar{2}$0) and M (10$\bar{1}$0) orientations is 4.2 ± 0.1 nm and 4.1 ± 0.1 nm, respectively. Moreover, the stacking distribution (Figure 11) displays a slightly higher stacking degree for A (11$\bar{2}$0) and M (10$\bar{1}$0) orientations (i.e., 1.3 compared to 1.1 for the R (1$\bar{1}$02) plane). These TEM observations are in good agreement with AFM data showing a larger slab size and height (i.e., stacking if one considers a basal bonding for MoS_2 nanoclusters) for A (11$\bar{2}$0) and M (10$\bar{1}$0) surfaces.

The different results (XPS, AFM, TEM) obtained on the sulfided model systems converge to show that two distinct behaviors are observed depending on the surface orientation. A (11$\bar{2}$0) and M (10$\bar{1}$0) surfaces show very similar characteristics with a high sulfidation degree of 78% and 87%, respectively, at 450 °C (XPS), similar MoS_2 slab length (slightly above 4 nm) and stacking, and identical molybdenum density (4 at. nm^{-2}). Conversely, the R (1$\bar{1}$02) plane shows a significantly lower sulfidation degree (60% at 450 °C) and shorter MoS_2 slabs (below 3 nm) with a slightly lower stacking. These results demonstrate a clear surface-dependent effect for

DOI: 10.1021/jacs.5b10975
J. Am. Chem. Soc. 2015, 137, 15915−15928

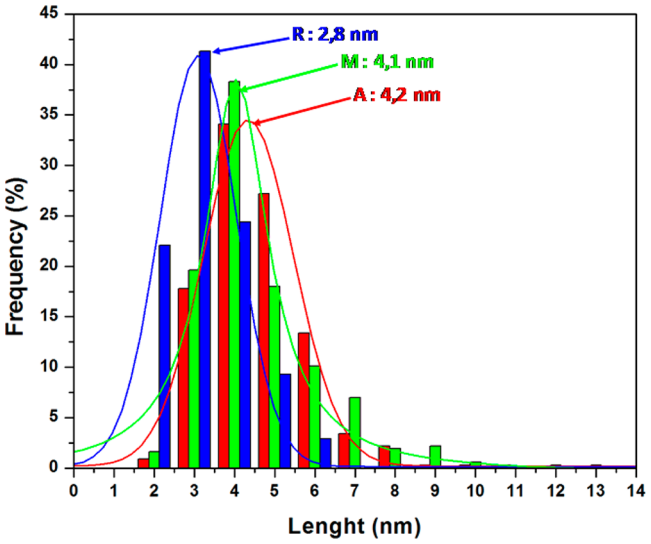

Figure 10. MoS_2 size distribution for model catalysts supported on A $(11\bar{2}0)$, M $(10\bar{1}0)$, and R $(1\bar{1}02)$ α-alumina single crystals sulfided at 450 °C for 2 h.

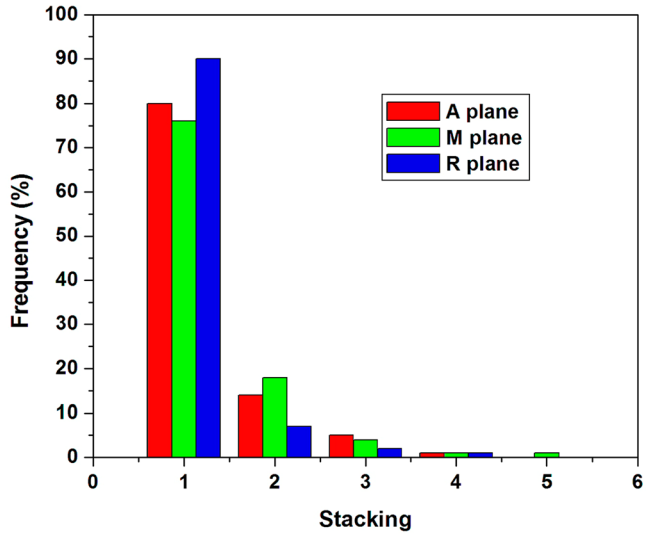

Figure 11. MoS_2 stacking distribution for model catalysts supported on A $(11\bar{2}0)$, M $(10\bar{1}0)$, and R $(1\bar{1}02)$ α-alumina single crystals sulfided at 450 °C for 2 h.

the speciation of the molybdenum sulfide nanostructure (size and sulfidation ratio).

The differences in sulfidation ratio may find two origins as shown in the seminal paper by Scheffer et al.:[74] the dispersion of the oxide Mo nanophase or its interaction with the support. Scheffer et al.[74] demonstrated that, for poorly dispersed, large MoO_3 particles, sulfidation may be limited by mass-transfer of H_2S in the sulfidation layer formed around the oxide core. Conversely, for highly dispersed particles, no mass-transfer limitations exist, and the sulfidation rate is mainly governed by the strength of metal−support interactions. As a matter of fact, it is well-known that Mo−O−Al bonds are broken during sulfidation leading to a substitution of oxygen with sulfur atoms. Hence, the strength of interaction between the active phase and the support via covalent Mo−O−Al linkage plays a fundamental role in the transformation of the oxide phase toward the sulfide phase. The higher the interaction strength is, the lower the sulfidation rate will be. Sakashita[75] confirmed this point by studying Mo catalysts supported on γ-alumina thin films with various surface orientations. The Mo sulfidation degree was decreasing in the following order: (110) > (100) > (111). This ranking was tentatively explained by a low oxygen density on the (110) plane and hence by a low number of Mo−O−Al bonds promoting a high degree of sulfidation while a larger number of Mo−O−Al bonds are formed on the (111) plane explaining a lower sulfidation ratio.

In the present case, variations in the sulfidation degree cannot be explained by an extremely different dispersion (i.e., size) of Mo nanoclusters at the oxide state. The different surfaces are actually differing by their Mo content (3−4 times higher on the A $(11\bar{2}0)$ and M $(10\bar{1}0)$ planes) which definitely plays a role in the Mo surface density (AFM and TEM show a larger surface coverage on the A $(11\bar{2}0)$ and M $(10\bar{1}0)$ planes) but with no drastic impact on the particle size. Actually, both AFM and TEM show that the sizes of MoS_2 nanoslabs on A $(11\bar{2}0)$, M $(10\bar{1}0)$, and R $(1\bar{1}02)$ planes are in the same range with an average height of about 0.5−2.0 nm (AFM) and a length of around 3−4 nm (TEM) with a lower length for the R $(1\bar{1}02)$ plane.

A different sulfidation ratio may then more probably arise from distinctive metal−support interactions on the various surfaces. High sulfidation rate on the A $(11\bar{2}0)$, M $(10\bar{1}0)$ facets suggests weaker Mo−O−Al bonds while stronger bonds would be involved on the R $(1\bar{1}02)$ plane leading to a lower sulfidation ratio. This hypothesis would also be in agreement with the formation of slightly smaller MoS_2 slabs on the R $(1\bar{1}02)$ surface since stronger bonds could limit the growth of MoS_2 slabs.[76] The evolution of the sulfidation ratio (Figure 6) is another indication for stronger metal−support interactions for the R plane versus A and M planes since the difference in sulfidation ratios is increasing with temperature. This behavior is in full agreement with the existence of hardly sulfidable Mo−O−Al bonds for the R plane that will resist high sulfidation temperature. If the differences in sulfidation ratio were related to differences in Mo dispersion (limited H_2S diffusion), one would expect a decreasing effect with temperature.

The surface chemistry (i.e., speciation of hydroxyl groups) of the various surface orientations may explain these differences. The R $(1\bar{1}02)$ plane exposes Al_{4c}-μ_1-OH surface sites as proposed by Tougerti et al.[19] Hence, low sulfidation rate on this surface might be explained by stronger Mo−O−Al bonds with these μ_1-OH surface sites as compared to bridged Al_{6c}-μ_n-OH (with n = 2 or 3) primarily exposed on the A $(11\bar{2}0)$ and M $(10\bar{1}0)$ orientations (Table 3). Singly coordinated surface OH species on the R $(1\bar{1}02)$ plane are probably preferentially exchanged due to their higher basicity (and consequently lability) with respect to bridged (μ_2 and μ_3) OH as shown by Digne et al.[77] for the preferential exchange of μ_1-OH groups by chloride anions on chlorinated alumina.

It has been shown previously (sections 1, 2, and 3) that A $(11\bar{2}0)$ and M $(10\bar{1}0)$ planes present high and similar reactivity toward Mo adsorption explained by identical surface OH groups (Al_{6c}-$\mu_{1,2,3}$-OH) and comparable surface structures. The R $(1\bar{1}02)$ plane is less reactive toward Mo adsorption due to a lower surface charge at the pH of adsorption. Hence, with a combination of the results of Mo adsorption at the oxide/water interface and sulfidation rate, it can be concluded that there are fewer adsorption sites on the R $(1\bar{1}02)$ plane but that these sites lead to stronger metal−support interaction.

DOI: 10.1021/jacs.5b10975
J. Am. Chem. Soc. 2015, 137, 15915−15928

As far as the orientation of the MoS_2 slabs is concerned, the results presented here do not provide explicit information. TEM analyses show slabs in side projection, but the preparation of the samples for TEM observation requires scraping the surface of the wafer which means that information on the orientation of the slabs with respect to the support is lost. AFM may be more conclusive since the 2D size of the MoS_2 particles is in good agreement with the length of a MoS_2 sheet in side projection as measured from TEM. This similarity could imply that MoS_2 slabs are lying flat on the surfaces investigated, but more work needs to be done to confirm this assumption.

6. Bridging the Gap with Real Catalysts. The conclusions drawn in the present work from model catalysts supported on α-Al_2O_3 wafers can be extended to real industrial Mo-based HDS catalysts supported on γ-Al_2O_3 since some relationship can be recognized between the surface groups exposed for both alumina polymorphs.

We showed recently[9] that the R $(1\bar{1}02)$ plane of α-Al_2O_3 can be taken as a partial model for the fully hydrated and predominant (110) surface of γ-Al_2O_3 (Scheme 2) since they

Scheme 2. Analogy between α-Alumina and γ-Alumina Surfaces Based on Experimental Data Presented in This Work

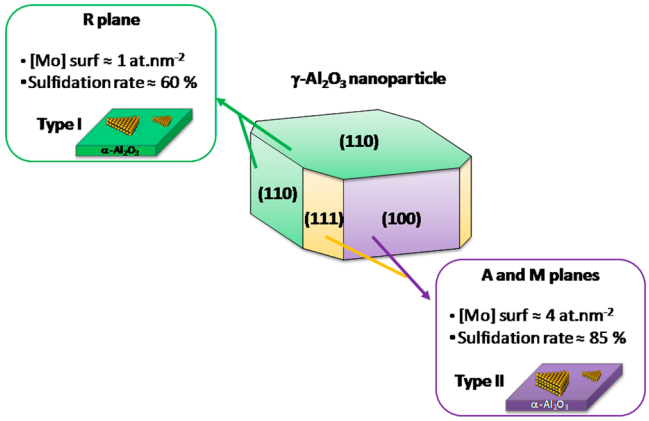

are both exposing Al_{4c}-μ_1-OH surface sites. It is however not a comprehensive model since the (110) γ-Al_2O_3 surface is also displaying Al_{5c}-μ_1-OH sites that are not present for α-Al_2O_3. A good agreement is also found between the A $(11\bar{2}0)$ plane (and therefore also the structurally related M $(10\bar{1}0)$ orientation) and the (100) γ-Al_2O_3 surface with both surfaces exposing Al_{6c}-μ_1-OH and Al_{6c}-μ_3-OH sites. A one-to-one relationship is less direct for the minor (111) γ-Al_2O_3 surface since it exposes several surface OH groups, but the closest match is found with the A $(11\bar{2}0)$ (and M $(10\bar{1}0)$) planes.[9] These considerations lead to a schematic description of γ-Al_2O_3 particles as modeled by the R $(1\bar{1}02)$ plane of α-Al_2O_3 for the (110) surface and by the A $(11\bar{2}0)$ and M $(10\bar{1}0)$ planes on the other hand for the (100) and (111) surfaces of γ-Al_2O_3 (Scheme 2).

Therefore, results obtained in this work suggest that Mo deposition on γ-Al_2O_3 will not result in homogeneous spreading of Mo on all γ-Al_2O_3 facets. Limited Mo adsorption occurs on the R $(1\bar{1}02)$ plane (about 1 Mo nm^{-2}) while extensive Mo adsorption occurs on the A $(11\bar{2}0)$ and M $(10\bar{1}0)$ planes (about 3−4 Mo nm^{-2}). Given the α-Al_2O_3/γ-Al_2O_3 relationship, (100) and (111) γ-Al_2O_3 surfaces should contain a higher density of Mo with respect to (110).

If one considers that the predominant (110) surface of γ-Al_2O_3 surface contributes to about 70% of the total surface area and only 30% for the (100) and (111) planes (such morphology is inherited from boehmite, the industrial hydrated precursor of γ-alumina),[17] a rough estimate of the Mo saturation at the pH of impregnation (i.e., pH = 5) leads to a maximum surface density of about 2 Mo nm^{-2} from the surface saturation of α-Al_2O_3 surfaces (Figure 1). This number is actually in good agreement with the Mo saturation coverage determined from an adsorption isotherm on powder γ-Al_2O_3 reported by Vissenberg et al.[78] (about 1.8 Mo nm^{-2}).

The sulfidation rate is also found to depend significantly on the α-Al_2O_3 surface. A $(11\bar{2}0)$ and M $(10\bar{1}0)$ surfaces show high sulfidation ratio of 80−85%, respectively, at 450 °C. Hence, the α-Al_2O_3/γ-Al_2O_3 analogy suggests a similar behavior for the (100) and (111) γ-Al_2O_3 planes that should concentrate most of the Mo fraction. In fact, these sulfidation ratios are in good agreement with those found on alumina powder in the same temperature range (sulfidation rate of about 85% at 400 °C according to Laurenti et al.[11]). A lower sulfidation ratio (60% at 450 °C) is found on the R $(1\bar{1}02)$ plane (i.e., the (110) γ-Al_2O_3 surface), but the Mo sulfidation rate on this orientation should be a minor contribution to the overall sulfidation rate for γ-Al_2O_3 since the Mo density on this surface is relatively low.

Lower sulfidation rate on the R $(1\bar{1}02)$ plane was assigned to the existence of stronger Mo−O−Al bonds which is also confirmed by slightly shorter MoS_2 slabs (below 3 nm) with respect to the other planes. The same behavior can thus be expected on the (110) γ-Al_2O_3 surface: shorter slabs with stronger metal−support interactions with respect to (100) and (111) orientations. These conclusions can be associated with the concept of type I/type II CoMoS structures first introduced by Candia et al.[79] and refined later on.[80] Type I molybdenum sulfide nanostructures present specific Mo−O−Al bonds with the support while type II structures are more weakly interacting with the support and lead to more active catalysts. Formation of Mo−O−Al bonds with the support increases the activation energy for the formation of sulfur vacancies, which can explain the lower HDS activity of type I catalysts.[80]

Our results suggest that type I and type II nanostructures may well exist on the same catalyst but be distributed among the various γ-Al_2O_3 surfaces. The sulfidation ratio of the R $(1\bar{1}02)$ plane (i.e., (110) γ-Al_2O_3 surface) can be associated with a type I structure while, for the other A $(11\bar{2}0)$ and M $(10\bar{1}0)$ orientations (i.e., (100) and (111) γ-Al_2O_3 surfaces), the sulfidation ratio is more consistent with type II structures (Scheme 2).

These results could indicate that a proper control of type I/type II structures may also involve careful control of the morphology of the oxide carrier.

■ CONCLUSIONS

Various surface orientations of planar α-Al_2O_3 single crystal wafers, C (0001), A $(11\bar{2}0)$, M $(10\bar{1}0)$, and R $(1\bar{1}02)$, were used for investigating the surface-dependent deposition and sulfidation of Mo in order to gain a deeper insight into support effects in hydrotreating catalysts.

First it has been shown that the Mo adsorption capacity of each surface orientation is governed by their surface structure and surface OH speciation that dictate the surface charge at the oxide/water interface: (i) the C (0001) surface is almost inert with negligible Mo adsorption; (ii) the R $(1\bar{1}02)$ surface is an

DOI: 10.1021/jacs.5b10975
J. Am. Chem. Soc. 2015, 137, 15915−15928

intermediate case with limited Mo adsorption (1 Mo nm^{-2}); and (iii) the A $(11\bar{2}0)$ and M $(10\bar{1}0)$ surfaces are highly reactive with a Mo surface density of 3−4 at. nm^{-2}. XANES suggests that adsorbed Mo nanoclusters at the oxide state are made of AHM-like edge-shared octahedra.

Sulfidation of the model catalysts also reveals salient differences among the various α-Al_2O_3 surfaces. High sulfidation rates are obtained for the A $(11\bar{2}0)$ and M $(10\bar{1}0)$ planes (78% and 87%, respectively) as opposed to the R $(1\bar{1}02)$ facet (60%). Moreover, slightly shorter MoS_2 slabs (about 3 nm) are obtained on the latter surface with respect to A $(11\bar{2}0)$ and M $(10\bar{1}0)$ surfaces. These results suggest stronger Mo−O−Al bonds for the R $(1\bar{1}02)$ plane that make sulfidation more difficult, but also reduce the MoS_2 slab size.

These results as well as analogies between α-Al_2O_3 and γ-Al_2O_3 surfaces allowed us to extend our conclusions to real γ-Al_2O_3-supported catalysts. It is proposed that Mo distribution as well as sulfidation degree are highly heterogeneous among various surface terminations of a single γ-Al_2O_3 particle in HDS catalysts (Scheme 2).

The present work shows that, among all methods which have been recently developed to improve the design of HDT catalysts (i.e., use of heteropolyanions (HPAs),[81] organic additives,[82−84] or mesoporous carriers[85]), the control of the support morphology appears as a key alternative to achieve a surface-dependent nanostructuration of the active phase.

■ ASSOCIATED CONTENT

Supporting Information

The Supporting Information is available free of charge on the ACS Publications website at DOI: 10.1021/jacs.5b10975.

Oxide phase characterization by AFM, details of DFT calculations for the A and M planes, and decomposition of S 2p XPS peak for sulfide catalysts (PDF)

■ AUTHOR INFORMATION

Corresponding Author

*E-mail: xavier.carrier@upmc.fr. Phone: +33 1 44 27 36 25. Fax: +33 1 44 27 60 33.

Notes

The authors declare no competing financial interest.

■ ACKNOWLEDGMENTS

We gratefully acknowledge C. Méthivier and C. Calers for assistance in XPS analysis, C. Domingos for technical support in adsorption experiments, and S. Casale for help in TEM experiments. We are also grateful to the SAMBA beamline staff at SOLEIL and especially to E. Fonda for his valuable assistance and expertise.

■ REFERENCES

(1) Toulhoat, H.; Raybaud, P. *Catalysis by Transition Metal Sulphides from Molecular Theory to Industrial Application*; IFP Énergies Nouvelles Publications, Technip, 2013.

(2) Furimsky, E. *Appl. Catal., A* **2000**, *199*, 147−190.

(3) Song, C. *Catal. Today* **2003**, *86*, 211−263.

(4) Topsøe, H.; Clausen, B. S.; Massoth, F. In *Catalysis Science and Technology*; Anderson, J. R., Boudart, M., Eds.; Springer: Berlin, 1996; Vol. *11*.

(5) Prins, R. In *Handbook of Heterogeneous Catalysis*; Ertl, G., Knözinger, H., Schüth, F., Eds.; Wiley-VCH Verlag: Weinheim, 1997; Vol. *4*.

(6) Topsøe, H.; Clausen, B. S.; Candia, R.; Wivel, C.; Mørup, S. *J. Catal.* **1981**, *68*, 433−452.

(7) Breysse, M.; Afanasiev, P.; Geantet, C.; Vrinat, M. *Catal. Today* **2003**, *86*, 5−16.

(8) Laurenti, D.; Devers, E. In *Catalysis by Transition Metal Sulphides from Molecular Theory to Industrial Application*; IFP Énergies Nouvelles Publications, Technip, 2013; pp 208−219.

(9) Bara, C.; Devers, E.; Digne, M.; Lamic-Humblot, A.-F.; Pirngruber, G.; Carrier, X. *ChemCatChem* **2015**, *7*, 3422−3440.

(10) Costa, D.; Arrouvel, C.; Breysse, M.; Toulhoat, H.; Raybaud, P. *J. Catal.* **2007**, *246*, 325−343.

(11) Laurenti, D.; Phung-Ngoc, B.; Roukoss, C.; Devers, E.; Marchand, K.; Massin, L.; Lemaitre, L.; Legens, C.; Quoineaud, A.-A.; Vrinat, M. *J. Catal.* **2013**, *297*, 165−175.

(12) Lauritsen, J.; Helveg, S.; Laegsgaard, E.; Stensgaard, I.; Clausen, B. S.; Topsøe, H.; Besenbacher, F. *J. Catal.* **2001**, *197*, 1−5.

(13) Lauritsen, J.; Kibsgaard, J.; Olesen, G.; Moses, P.; Hinnemann, B.; Helveg, S.; Nørskov, J.; Clausen, B.; Topsøe, H.; Lagsgaard, E.; Besenbacher, F. *J. Catal.* **2007**, *249*, 220−233.

(14) Kibsgaard, J.; Clausen, B. S.; Topsøe, H.; Lægsgaard, E.; Lauritsen, J. V.; Besenbacher, F. *J. Catal.* **2009**, *263*, 98−103.

(15) Sakashita, Y.; Yoneda, T. *J. Catal.* **1999**, *185*, 487−495.

(16) Sterrer, M.; Freund, H.-J. *Catal. Lett.* **2013**, *143*, 375−385.

(17) Digne, M.; Sautet, P.; Raybaud, P.; Euzen, P.; Toulhoat, H. *J. Catal.* **2004**, *226*, 54−68.

(18) Marmier, A.; Parker, S. C. *Phys. Rev. B: Condens. Matter Mater. Phys.* **2004**, *69*, 115409-1−115409-9.

(19) Tougerti, A.; Méthivier, C.; Cristol, S.; Tielens, F.; Che, M.; Carrier, X. *Phys. Chem. Chem. Phys.* **2011**, *13*, 6531−6543.

(20) Hass, K. C.; Schneider, W. F.; Curioni, A.; Andreoni, W. *Science* **1998**, *282*, 265−268.

(21) Eng, P. J.; Trainor, T. P.; Brown, G. E., Jr; Waychunas, G. A.; Newville, M.; Sutton, S. R.; Rivers, M. L. *Science* **2000**, *288*, 1029−1033.

(22) Trainor, T. P.; Eng, P. J.; Brown, G. E., Jr; Robinson, I. K.; Santis, M. D. *Surf. Sci.* **2002**, *496*, 238−250.

(23) Catalano, J. G. *Geochim. Cosmochim. Acta* **2011**, *75*, 2062−2071.

(24) Catalano, J. G.; Fenter, P.; Park, C. *Geochim. Cosmochim. Acta* **2009**, *73*, 2242−2251.

(25) Catalano, J. G.; Park, C.; Zhang, Z.; Fenter, P. *Langmuir* **2006**, *22*, 4668−4673.

(26) Catalano, J. G. *J. Phys. Chem. C* **2010**, *114*, 6624−6630.

(27) Lambert, J.-F.; Che, M. *J. Mol. Catal. A: Chem.* **2000**, *162*, 5−18.

(28) Fairley, N. *CasaXPS Version 2.3.12*; Casa Software Ltd., 2006.

(29) Towle, S. N.; Bargar, J. R.; Brown, G. E.; Parks, G. A. *J. Colloid Interface Sci.* **1999**, *217*, 312−321.

(30) Gandubert, A. D.; Legens, C.; Guillaume, D.; Payen, E. *Surf. Interface Anal.* **2006**, *38*, 206−209.

(31) Lamic-Humblot, A.-F.; Barthe, P.; Guzman, G.; Delannoy, L.; Louis, C. *Thin Solid Films* **2013**, *527*, 96−101.

(32) Schneider, C. A.; Rasband, W. S.; Eliceiri, K. W. *Nat. Methods* **2012**, *9*, 671−675.

(33) Kresse, G.; Furthmuller, J. *Phys. Rev. B: Condens. Matter Mater. Phys.* **1996**, *54*, 11169−11186.

(34) Kresse, G.; Hafner, J. *Phys. Rev. B: Condens. Matter Mater. Phys.* **1994**, *49*, 14251−14269.

(35) Perdew, J. P.; Burke, K.; Ernzerhof, M. *Phys. Rev. Lett.* **1996**, *77*, 3865−3868.

(36) Kresse, G.; Joubert, D. *Phys. Rev. B: Condens. Matter Mater. Phys.* **1999**, *59*, 1758−1775.

(37) Digne, M.; Sautet, P.; Raybaud, P.; Euzen, P.; Toulhoat, H. *J. Catal.* **2002**, *211*, 1−5.

(38) Adamcik, J.; Berquand, A.; Mezzenga, R. *Appl. Phys. Lett.* **2011**, *98*, 193701-1−193701-3.

(39) Baudelet, F.; Belkhou, R.; Briois, V.; Coati, A.; Dumas, P.; Etgens, V.; Flank, A. M.; Fontaine, P.; Garreau, Y.; Quinkal, I.; Rochet, F.; Roy, P.; Sauvage, M.; Sirotti, F.; Somogyi, A.; Thiaudère, D. *Oil Gas Sci. Technol.* **2005**, *60*, 849−874.

DOI: 10.1021/jacs.5b10975
J. Am. Chem. Soc. 2015, 137, 15915−15928

(40) Ravel, B.; Newville, M. *J. Synchrotron Radiat.* **2005**, *12*, 537−541.
(41) Kitayama, M.; Glaeser, A. M. *J. Am. Ceram. Soc.* **2002**, *85*, 611−622.
(42) Heald, S. M.; Keller, E.; Stern, E. A. *Phys. Lett. A* **1984**, *103A*, 155−158.
(43) Tougerti, A.; Berrier, E.; Mamede, A.-S.; La Fontaine, C.; Briois, V.; Joly, Y.; Payen, E.; Paul, J.-F.; Cristol, S. *Angew. Chem., Int. Ed.* **2013**, *52*, 6440−6444.
(44) Wang, X.-L.; Hubbard, C. R.; Alexander, K. B.; Becher, P. F.; Fernandez-Baca, J. A.; Spooner, S. *J. Am. Ceram. Soc.* **1994**, *77*, 1569−1575.
(45) Raybaud, P.; Digne, M.; Iftimie, R.; Wellens, W.; Euzen, P.; Toulhoat, H. *J. Catal.* **2001**, *201*, 236−246.
(46) Spanos, N.; Vordonis, L.; Kordulis, C.; Lycourghiotis, A. *J. Catal.* **1990**, *124*, 301−314.
(47) Spanos, N.; Vordonis, L.; Kordulis, C.; Koutsoukos, P. G.; Lycourghiotis, A. *J. Catal.* **1990**, *124*, 315−323.
(48) Bourikas, K.; Kordulis, C.; Lycourghiotis, A. *Catal. Rev.: Sci. Eng.* **2006**, *48*, 363−344.
(49) Lützenkirchen, J.; Zimmermann, R.; Preočanin, T.; Filby, A.; Kupcik, T.; Küttner, D.; Abdelmonem, A.; Schild, D.; Rabung, T.; Plaschke, M.; Brandenstein, F.; Werner, C.; Geckeis, H. *Adv. Colloid Interface Sci.* **2010**, *157*, 61−74.
(50) Lützenkirchen, J. *Langmuir* **2013**, *29*, 7726−7734.
(51) Hiemstra, T.; Venema, P.; van Riemsdijk, W. H. *J. Colloid Interface Sci.* **1996**, *184*, 680−692.
(52) Fitts, J. P.; Shang, X.; Flynn, G. W.; Heinz, T. F.; Eisenthal, K. B. *J. Phys. Chem. B* **2005**, *109*, 7981−7986.
(53) Zhang, L.; Tian, C.; Waychunas, G. A.; Shen, Y. R. *J. Am. Chem. Soc.* **2008**, *130*, 7686−7694.
(54) Flörsheimer, M.; Kruse, K.; Polly, R.; Abdelmonem, A.; Schimmelpfennig, B.; Klenze, R.; Fanghänel, T. *Langmuir* **2008**, *24*, 13434−13439.
(55) Yong, H.; Van Riemsdijk, W. H. *Langmuir* **1999**, *15*, 5942−5955.
(56) Hiemstra, T.; Van Riemsdijk, W. H.; Bolt, G. H. *J. Colloid Interface Sci.* **1989**, *133*, 91−104.
(57) Hiemstra, T.; De Wit, J. C. M.; Van Riemsdijk, W. H. *J. Colloid Interface Sci.* **1989**, *133*, 105−117.
(58) Sung, J.; Zhang, L.; Tian, C.; Shen, Y. R.; Waychunas, G. A. *J. Phys. Chem. C* **2011**, *115*, 13887−13893.
(59) Contescu, C.; Jagiello, J.; Schwarz, J. A. *Langmuir* **1993**, *9*, 1754−1765.
(60) Sung, J.; Shen, Y. R.; Waychunas, G. A. *J. Phys.: Condens. Matter* **2012**, *24*, 124101-1−124101-9.
(61) Bargar, J. R.; Towle, S. N.; Brown, G. E., Jr.; Parks, G. A. *Geochim. Cosmochim. Acta* **1996**, *60*, 3541−3547.
(62) Bargar, J. R.; Towle, S. N.; Brown, G. E.; Parks, G. A. *J. Colloid Interface Sci.* **1997**, *185*, 473−492.
(63) Tougerti, A.; Llorens, I.; D'Acapito, F.; Fonda, E.; Hazemann, J.-L.; Joly, Y.; Thiaudière, D.; Che, M.; Carrier, X. *Angew. Chem., Int. Ed.* **2012**, *51*, 7697−7701.
(64) Gandubert, A. D.; Legens, C.; Guillaume, D.; Rebours, S.; Payen, E. *Oil Gas Sci. Technol.* **2007**, *62*, 79−89.
(65) Gandubert, A. D.; Krebs, E.; Legens, C.; Costa, D.; Guillaume, D.; Raybaud, P. *Catal. Today* **2008**, *130*, 149−159.
(66) Coulier, L.; De Beer, V. H. J.; Van Veen, J. A. R.; Niemantsverdriet, J. W. *Top. Catal.* **2000**, *13*, 99−108.
(67) Weber, T.; Muijsers, J. C.; Niemantsverdriet, J. W. *J. Phys. Chem.* **1995**, *99*, 9194−9200.
(68) Galtayries, A.; Wisniewski, S.; Grimblot, J. *J. Electron Spectrosc. Relat. Phenom.* **1997**, *87*, 31−44.
(69) Dupin, J. C.; Gonbeau, D.; Martin-Litas, I.; Vinatier, P.; Levasseur, A. *Appl. Surf. Sci.* **2001**, *173*, 140−150.
(70) Venezia, A. M. *Catal. Today* **2003**, *77*, 359−370.
(71) Nečas, D.; Klapetek, P. *Open Phys.* **2012**, *10*, 181−188.
(72) Schweiger, H.; Raybaud, P.; Kresse, G.; Toulhoat, H. *J. Catal.* **2002**, *207*, 76−87.
(73) Vrinat, M.; Breysse, M.; Geantet, C.; Ramirez, J.; Massoth, F. *Catal. Lett.* **1994**, *26*, 25−35.
(74) Scheffer, B.; Arnoldy, P.; Moulijn, J. A. *J. Catal.* **1988**, *112*, 516−527.
(75) Sakashita, Y. *Surf. Sci.* **2001**, *489*, 45−58.
(76) Ramirez, J.; Fuentes, S.; Díaz, G.; Vrinat, M.; Breysse, M.; Lacroix, M. *Appl. Catal.* **1989**, *52*, 211−224.
(77) Digne, M.; Raybaud, P.; Sautet, P.; Guillaume, D.; Toulhoat, H. *J. Am. Chem. Soc.* **2008**, *130*, 11030−11039.
(78) Vissenberg, M. J.; Joosten, L. J. M.; Heffels, M. M. E. H.; van Welsenes, A. J.; de Beer, V. H. J.; van Santen, R. A.; van Veen, J. A. R. *J. Phys. Chem. B* **2000**, *104*, 8456−8461.
(79) Candia, R.; Soerensen, O.; Villadsen, J.; Topsøe, N. Y.; Clausen, B. S.; Topsøe, H. *Bull. Soc. Chim. Belg.* **1984**, *93*, 763−773.
(80) Hinnemann, B.; Nørskov, J. K.; Topsøe, H. *J. Phys. Chem. B* **2005**, *109*, 2245−2253.
(81) Mazurelle, J.; Lamonier, C.; Lancelot, C.; Payen, E.; Pichon, C.; Guillaume, D. *Catal. Today* **2008**, *130*, 41−49.
(82) Bergwerff, J. A.; Jansen, M.; Leliveld, B. G.; Visser, T.; de Jong, K. P.; Weckhuysen, B. M. *J. Catal.* **2006**, *243*, 292−302.
(83) Fremon, B.; Chaumonnot, A.; Marchand, K.; Payen, E. *Stud. Surf. Sci. Catal.* **2006**, *162*, 291−298.
(84) Texier, S.; Berhault, G.; Perot, G.; Harle, V.; Diehl, F. *J. Catal.* **2004**, *223*, 404−418.
(85) Sampieri, A.; Pronier, S.; Brunet, S.; Carrier, X.; Louis, C.; Blanchard, J.; Fajerwerg, K.; Breysse, M. *Microporous Mesoporous Mater.* **2010**, *130*, 130−141.

DOI: 10.1021/jacs.5b10975
J. Am. Chem. Soc. 2015, 137, 15915−15928